



Activation of autophagy by *in situ* Zn²⁺ chelation reaction for enhanced tumor chemoimmunotherapy

Yang Yang^{a,b,1}, Yefei Zhu^{a,1}, Kairuo Wang^{a,1}, Yunqiu Miao^a, Yuanyuan Zhang^a, Jie Gao^{c,**}, Huanlong Qin^{a,***}, Yang Zhang^{a,b,*}

^a Nanomedicine and Intestinal Microecology Research Center, Shanghai Tenth People's Hospital, School of Medicine, Tongji University, Shanghai, 200072, PR China

^b School of Medicine, Shanghai University, Shanghai, 200444, PR China

^c Changhai Clinical Research Unit, Shanghai Changhai Hospital, Naval Medical University, Shanghai, 200433, PR China

ARTICLE INFO

Keywords:

Chemoimmunotherapy
Immunogenic cell death (ICD)
Damage-associated molecular patterns (DAMPs)
Autophagy
In situ chelation

ABSTRACT

Chemotherapy can induce a robust T cell antitumor immune response by triggering immunogenic cell death (ICD), a process in which tumor cells convert from nonimmunogenic to immunogenic forms. However, the antitumor immune response of ICD remains limited due to the low immunogenicity of tumor cells and the immunosuppressive tumor microenvironment. Although autophagy is involved in activating tumor immunity, the synergistic role of autophagy in ICD remains elusive and challenging. Herein, we report an autophagy amplification strategy using an ion-chelation reaction to augment chemoimmunotherapy in cancer treatments based on zinc ion (Zn²⁺)-doped, disulfiram (DSF)-loaded mesoporous silica nanoparticles (DSF@Zn-DMSNs). Upon pH-sensitive biodegradation of DSF@Zn-DMSNs, Zn²⁺ and DSF are coreleased in the mildly acidic tumor microenvironment, leading to the formation of toxic Zn²⁺ chelate through an *in situ* chelation reaction. Consequently, this chelate not only significantly stimulates cellular apoptosis and generates damage-associated molecular patterns (DAMPs) but also activates autophagy, which mediates the amplified release of DAMPs to enhance ICD. *In vivo* results demonstrated that DSF@Zn-DMSNs exhibit strong therapeutic efficacy via *in situ* ion chelation and possess the ability to activate autophagy, thus enhancing immunotherapy by promoting the infiltration of T cells. This study provides a smart *in situ* chelation strategy with tumor microenvironment-responsive autophagy amplification to achieve high tumor chemoimmunotherapy efficacy and biosafety.

1. Introduction

Cancer chemotherapy drugs have long been considered immunosuppressive and can weaken the immune system [1,2]. However, more recent data indicate that chemotherapy could elicit antitumor immunity by inducing immunogenic cell death (ICD) of tumor cells. ICD refers to a process of regulated cell death triggered by external stimuli that transforms tumor cells from a nonimmunogenic to an immunogenic state, synthesizing and releasing damage-associated molecular patterns (DAMPs), including calreticulin (CRT), high mobility group box 1

(HMGB1), adenosine triphosphate (ATP), and heat shock proteins (HSPs) [3–5]. ICD can mobilize antigen-presenting cells (APCs), improve infiltration of cytotoxic T lymphocytes (CTLs) and thus trigger a systemic antitumor immune response [6]. However, the antitumor immune response of ICD remains limited due to the low immunogenicity of tumor cells and the immunosuppressive tumor microenvironment (TME), which contributes to immune escape effects and tumor progression [7,8]. Consequently, developing strategies to enhance ICD efficiency, boost tumor immunogenicity, and reprogram the TME has become a major area of research interest to improve the overall efficacy

Peer review under responsibility of KeAi Communications Co., Ltd.

* Corresponding author. Nanomedicine and Intestinal Microecology Research Center, Shanghai Tenth People's Hospital, School of Medicine, Tongji University, Shanghai, 200072, PR China.

** Corresponding author. Changhai Clinical Research Unit, Shanghai Changhai Hospital, Naval Medical University, Shanghai, 200433, PR China.

*** Corresponding author. Nanomedicine and Intestinal Microecology Research Center, Shanghai Tenth People's Hospital, School of Medicine, Tongji University, Shanghai, 200072, PR China.

E-mail addresses: gaojiehighclea@smmu.edu.cn (J. Gao), hlongqin@126.com (H. Qin), zhangyang0202@tongji.edu.cn (Y. Zhang).

¹ These authors contributed equally to this work.

<https://doi.org/10.1016/j.bioactmat.2023.06.022>

Received 21 April 2023; Received in revised form 21 June 2023; Accepted 26 June 2023

2452-199X/© 2023 The Authors. Publishing services by Elsevier B.V. on behalf of KeAi Communications Co. Ltd. This is an open access article under the CC BY-NC-ND license (<http://creativecommons.org/licenses/by-nc-nd/4.0/>).

of immunotherapy.

In recent years, the relationship between autophagy and tumor immunity has gradually been uncovered [9]. Autophagy is a multistep lysosome-mediated process that supports nutrient cycling and metabolic adaptation, and it has been implicated in the initiation and progression of cancers [10,11]. Additionally, autophagy plays a crucial role in facilitating the expression of MHC-I molecules on the cytomembrane, enabling them to be recognized by T cell receptors on CTLs [12]. Moreover, tumor cell-released autophagosomes (TRAPs) have been found to impact the immunological function of various immune cells, such as B cells, macrophages, and neutrophils [13–15]. Furthermore, active ATP secretion is linked to autophagy, as it promotes the migration of ATP-containing lysosomes toward the plasma membrane [16]. Additionally, other DAMPs originating from dying tumor cells can be presented to APCs during autophagic cell death [17]. Therefore, rational intervention in the autophagy process emerges as an effective approach to enhance tumor chemoimmunotherapy.

Disulfiram (DSF), a Food and Drug Administration (FDA)-approved anti-alcoholic drug with low toxicity, has recently been utilized in cancer therapy [18]. It has been demonstrated that the antitumor effects of DSF are dependent on certain metals, such as Cu^{2+} , Zn^{2+} , and Ni^{2+} [19,20]. In a physical environment, DSF is metabolized into dithiocarbamate (DTC), and the disulfide dimer present in DSF actively chelates metals to form toxicity complexes, ultimately leading to cellular apoptosis [18,21]. For instance, the combination of DSF and copper in tumor therapy has been investigated along with its associated mechanism. This combination disables the essential p97-NPL4-UFD1 pathway,

activates the mitogen-activated protein kinase (MAPK) signaling pathway, and induces autophagic cell death [22–25]. However, the toxicity of copper to normal tissues limits its application. Zinc ions (Zn^{2+}), which are essential trace elements in the human body, play a critical role as components or activators of vital enzymes and participate in various physiological processes. Recent research has revealed that excessive intracellular Zn^{2+} can activate autophagy signaling pathways and disrupt intracellular environmental homeostasis [26]. Based on these findings, it is hypothesized that combining Zn^{2+} and DSF in tumor therapy can convert nontoxic substances into toxic substances through *in situ* chelation reactions. This process induces tumor cell apoptosis while minimizing toxicity to normal tissues. Additionally, it activates tumor cell autophagy to promote antigen release and presentation, thereby enhancing immunotherapy.

However, the concentration of Zn^{2+} in the physiological environment is insufficient to produce enough toxic DTC-Zn complexes, and the poor hydrophobicity and strong toxicity of DTC-Zn complexes limit their direct application as a therapeutic drug [27]. Herein, Zn^{2+} -doped dendritic mesoporous silica nanoparticles (designated Zn-DMSNs) were rationally designed and fabricated and then loaded with DSF (designated DSF@Zn-DMSNs) to achieve pH-triggered Zn^{2+} release, efficient delivery of DSF, and activation of autophagy for tumor immunotherapy specifically targeting tumors (Fig. 1a). After the entry of DSF@Zn-DMSNs into tumors, DMSNs first responded to the acidic microenvironment and released loaded Zn^{2+} and DSF. Then, the *in situ* chelation reaction between Zn^{2+} and DTC generates toxic products that induce tumor cell apoptosis, while the overloaded Zn^{2+} activates tumor

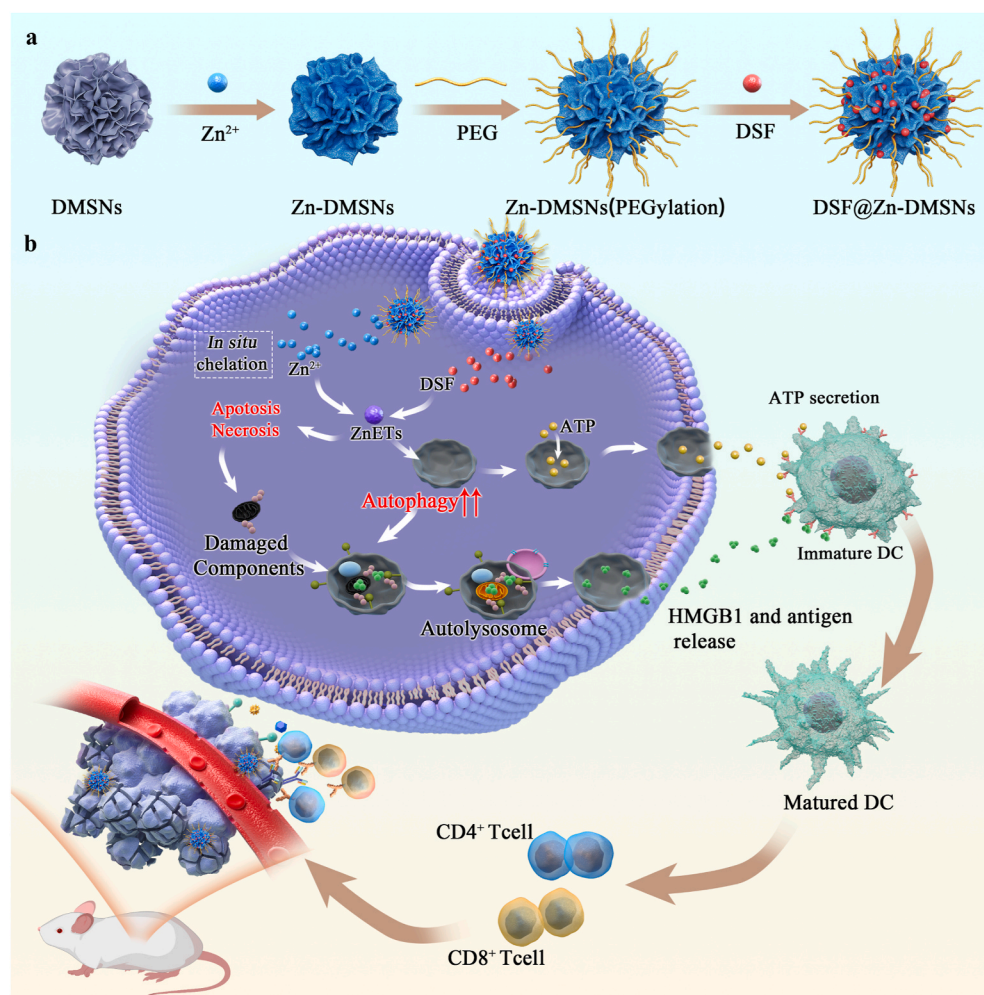


Fig. 1. Schematic diagram of the construction of DSF@Zn-DMSNs for enhanced chemoimmunotherapy in cancer treatments. (a) To elaborate the efficiency of immunotherapy during chemotherapy, the as-designed autophagy-amplified Zn^{2+} -doped, disulfiram (DSF)-loaded mesoporous silica nanoparticles (DSF@Zn-DMSNs) were synthesized based on biological responsiveness, with homogeneous *in situ* growth of Zn^{2+} into the pores of DMSNs and loading of DSF into Zn-DMSNs. (b) The ZnETs generated by the *in situ* chelation reaction of Zn^{2+} and DSF released from the degradation of DSF@Zn-DMSNs in the acidic tumor microenvironment could induce apoptosis and necrosis in tumors, while they can also activate autophagy to release DAMPs (ATP, HMGB1, etc.) to stimulate ICD, thereby enhancing chemoimmunotherapy in cancer treatment.

cell autophagy, which enhances the release of DAMPs (Fig. 1b). Moreover, *in vivo* experiments demonstrated that DSF@Zn-DMSNs enhanced autophagy expression and T cell recruitment in tumors, leading to efficient antitumor therapy with no significant toxicity to other organs. This study provides a TME-responsive autophagy amplification platform to augment tumor chemoimmunotherapy with increased antitumor efficacy and reduced systemic toxicity.

2. Results and discussion

2.1. Design, synthesis, and characteristics of DSF@Zn-DMSNs

To endow the nanodelivery system with autophagy activation and improve the effectiveness of DSF chemotherapy, especially in the TME, Zn²⁺-doped dendritic mesoporous silica nanoparticles (designated Zn-DMSNs) were rationally fabricated by a hydrothermal method and then loaded with DSF (designated DSF@Zn-DMSNs) [21]. Transmission electron microscopy (TEM) and scanning electron microscopy (SEM)

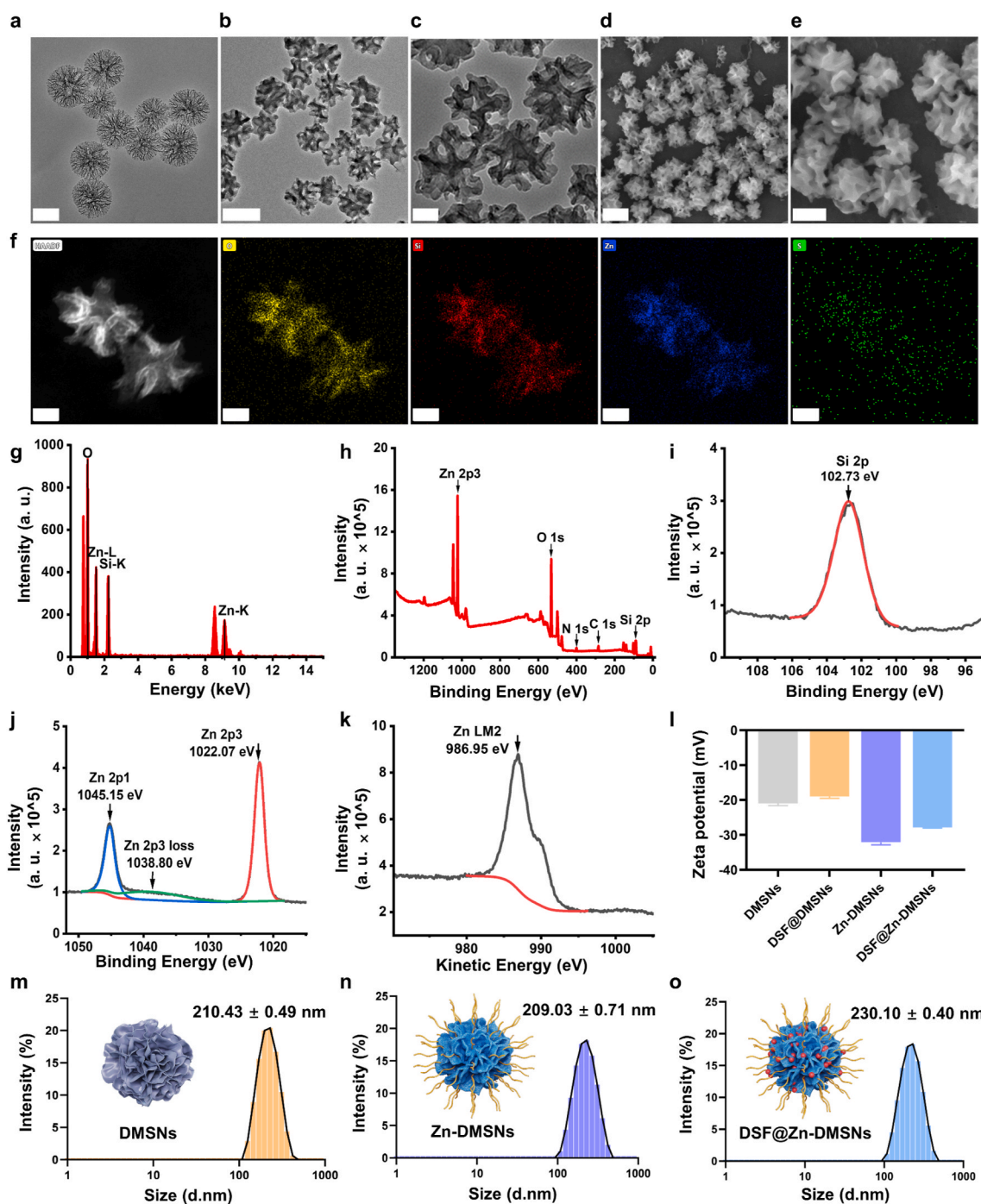


Fig. 2. Structure and characteristics of Zn-DMSNs and DSF@Zn-DMSNs. (a) TEM images of DMSNs, scale bar = 200 nm. (b) and (c) TEM images of DSF@Zn-DMSNs; scale bar: 200 nm (b) and 50 nm (c). (d) and (e) SEM images of DSF@Zn-DMSNs; scale bar: 200 nm (d) and 100 nm (e). (f) Elemental mapping of DSF@Zn-DMSNs; scale bar: 50 nm. (g) EDS of DSF@Zn-DMSNs. (h–j) Zn-DMSNs XPS spectra at different binding energies. (k) Auger electron spectroscopy of Zn-DMSNs. (l) Zeta potential of DMSNs, DSF@DMSNs, Zn-DMSNs, and DSF@Zn-DMSNs. (m–o) Size distribution graph of DMSNs (m), Zn-DMSNs (n), and DSF@Zn-DMSNs (o).

showed that DMSNs were monodisperse with a central-radial dendritic structure and ultralarge radial pores (Fig. 2a and Fig. S1). Compared with DMSNs, Zn-DMSNs showed a larger pore structure and thicker hole wall (Fig. 2b–e and Fig. S2), which provided the possibility for the incorporation of a larger amount of DSF. Under hydrothermal conditions, as soon as the unsubstantial mesoporous walls of DMSNs were dissolved in $\text{NH}_3\cdot\text{H}_2\text{O}$, they released silica oligomers capable of reacting with the Zn^{2+} precursors ($\text{Zn}(\text{NO}_3)_2\cdot 6\text{H}_2\text{O}$) to generate a Zn^{2+} -doped silicon (Si) layer covering the undissolved pore walls, thereby creating larger pore channels and thicker pore walls. Scanning transmission electron microscopy dark-field (STEM-DF) images and elemental mapping also revealed the successful immobilization of Zn^{2+} into the pore walls (Fig. 2f). The atomic ratio of Zn/Si was calculated to be 59.4% according to the Zn and Si signals in the energy dispersive spectrometer (EDS) (Fig. 2g). Such high Zn loading can contribute to the release of more Zn^{2+} in the tumor tissue for *in situ* production of toxic DTC-Zn complexes and activation of tumor cell autophagy. X-ray photoelectron spectroscopy (XPS) and Auger electron spectroscopy (AES) sputter depth profiling were utilized to further analyze the valence states of Zn and Si in DSF@Zn-DMSNs, and the results clearly showed the signals of Si and Zn (Fig. 2h). The Si 2p peak at 102.73 eV was attributed to Si–O bonds (Fig. 2i). The binding energies of Zn 2p at 1022.07 eV, 1038.80 eV, and 1045.15 eV corresponded to metallic zinc (ZnII) (Fig. 2j). The AES result confirmed that the peak of Zn LM2 was at 986.95 eV. The Auger parameter of Zn, which was the sum of its kinetic energy and binding energy, was close to the Auger parameter of $\text{Zn}_4\text{Si}_2\text{O}_7(\text{OH})_2$ and ZnO (Fig. 2k), confirming the presence of Zn–O bonds in the synthetic Zn-DMSNs. Furthermore, ICP–OES also confirmed successful Zn^{2+} doping and DSF loading (Table S1). The weight content of Zn^{2+} was 26.4%, while the loading efficiency of DSF in our DSF@Zn-DMSNs was approximately 9.4%.

Then, zeta potential measurements were conducted (Fig. 2l), and the results showed that the synthesized DMSNs were negatively charged (zeta potential: -20.96 mV) due to the abundance of silanol groups, thus promoting the adsorption of DSF. The zeta potentials of DSF@DMSNs,

Zn-DMSNs, and DSF@Zn-DMSNs were -18.99 mV, -32.10 mV and -27.89 mV, respectively. Compared to DMSNs or Zn-DMSNs, the slight increase in potential in DSF@DMSNs or DSF@Zn-DMSNs might be due to the loading of DSF. Compared to the DMSNs, the significant decrease in zeta potential in Zn-DMSNs indicated the success of Zn^{2+} immobilization. Dynamic light scattering (DLS) results showed that the average particle sizes of DMSNs, Zn-DMSNs and DSF@Zn-DMSNs were 210.43 ± 0.49 nm, 209.03 ± 0.71 nm and 230.10 ± 0.40 nm, respectively (Fig. 2m–o). DMEM completely simulates physiological conditions more closely and is often used in *in vitro* and *in vivo* experiments. We then examined the stability of the nanoparticles in water (Fig. S3a) and complete DMEM containing 10% FBS (Fig. S3b) every day over a period of 14 consecutive days via DLS analysis. Our results show that the nanoparticles maintained their stability in these media throughout this period, which we believe demonstrates their robustness and applicability in various environments.

2.2. *In vitro* biodegradability evaluation of Zn-DMSNs

Previous studies have proven that Zn–O bonds are easy to break under mildly acidic conditions in the TME [28,29]. Therefore, the presence of Zn–O bonds in the skeleton of the Zn-DMSNs carrier could contribute to structural degradation and Zn^{2+} ion release under mildly acidic conditions, which further promoted the chelation reaction of Zn^{2+} and surface-loaded DSF *in situ*. To verify the hypothesis that Zn-DMSNs degrade under mildly acidic conditions, Zn-DMSNs were dispersed in simulated body fluid (SBF) solutions at different pH levels to mimic their biodegradation *in vitro*. We evaluated the degradation process using ICP–OES and TEM images. The Zn-DMSNs morphology and structural evolution were monitored directly using TEM images (Fig. 3a). The structure of the nanoparticles remained nearly intact after a 4-h incubation in both acidic (pH 6.5) and neutral (pH 7.4) SBF solutions compared to their initial states. The nanostructure of Zn-DMSNs incubated with the neutral SBF solution (pH 7.4) for 24 h displayed the highest level of morphological integrity until significant deformations

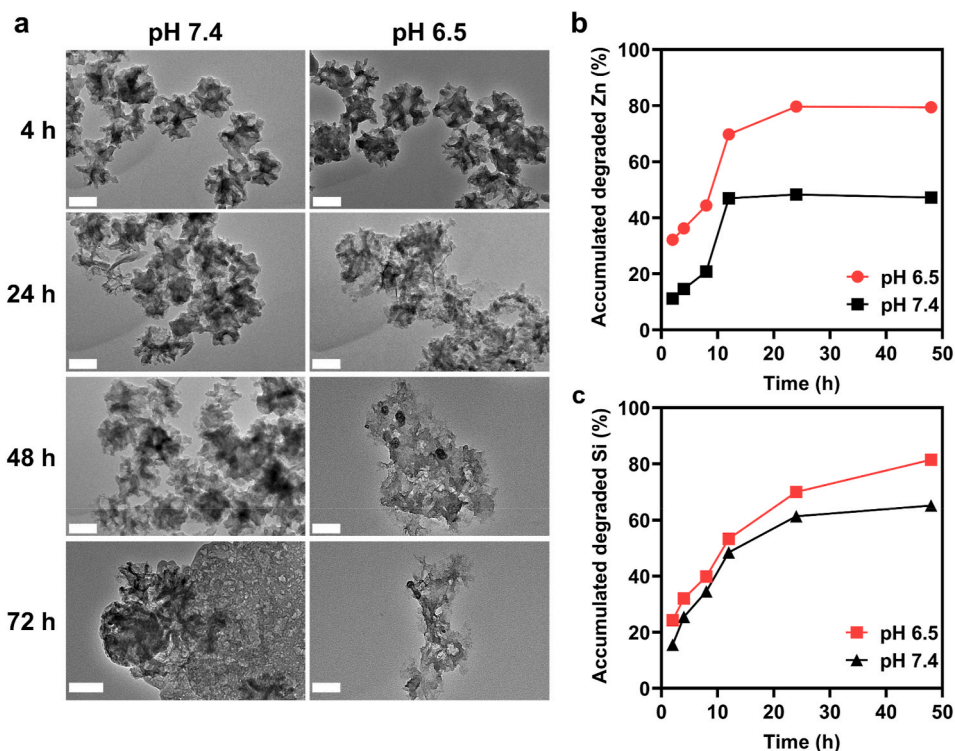


Fig. 3. Biodegradability evaluation of Zn-DMSNs. (a) TEM images of Zn-DMSNs immersed in SPB solutions with different pH levels for 4, 24, 48 and 72 h; scale bar: 100 nm. The accumulation of degraded Zn (b) and Si (c) from Zn-DMSNs immersed in SBF with different pH levels.

were observed at the 48 h time point. In contrast, the Zn-DMSNs in an acidic SBF solution (pH 6.5) began to collapse after 24 h of incubation, became aberrantly aggregated at the 24 h time point, and left remarkable debris at the 48 h and 72 h time points. In addition, the Zn²⁺ ion release ratio of the nanoparticles under mildly acidic conditions was faster than that under neutral conditions (Fig. 3b). This fact further verified that the Zn–O bonds were easily attacked by H⁺. The rapid release of Zn²⁺ ions from the Zn-DMSNs framework caused additional defects to appear, and the release of Si occurred as a result of accelerated nanostructure disintegration (Fig. 3b and c). To verify the generation of ZnET, the DSF@Zn-DMSNs were immersed in SBF (pH 6.5) for 2 weeks to fully release Zn²⁺ and DSF and form ZnET. We simulated the intracellular reductive conditions using 5 mM glutathione (GSH) as a reducing agent because disulfiram (DSF) was unable to chelate Zn²⁺ unless the disulfide bond was cleaved under reductive conditions, while one of the characteristics of the TME is high GSH. Zn-DMSNs were used as a negative control. After 14 days of degradation, the degraded products were then collected for DLS, TEM, and EDS analysis. The average size of the degradation products of DSF@Zn-DMSNs was 3506 ± 81.5 nm (Fig. S4). The TEM result of the degraded product of Zn-DMSNs (Fig. S5a) and DSF@Zn-DMSNs (Fig. S5b). The corresponding EDS spectra showed that both Zn and Si were present in the degradation products of Zn-DMSNs (Fig. S5c) and DSF@Zn-DMSNs (Fig. S5d),

while significant signals of S were observed in the degradation products of DSF@Zn-DMSNs (Fig. S5d), indicating the generation of ZnET.

2.3. The cytotoxicity of nanoparticles against murine colorectal cancer cells

To investigate the cellular uptake of DMSNs and Zn-DMSNs in CT-26 murine colorectal carcinoma cells, the nanoparticles were labeled with fluorescein isothiocyanate (FITC), and fluorescence microscopy was utilized to track the internalization of these FITC-labeled nanoparticles inside the CT-26 cells (Fig. 4a and b) [30]. The results revealed that the green fluorescence intensity in the Zn-DMSNs and DMSNs groups gradually increased in a time-dependent manner and did not show obvious differences, suggesting that both DMSNs and Zn-DMSNs showed similar uptake efficacy in colorectal cancer cells. The cytotoxicity of nanoparticles was tested using a cell counting kit-8 (CCK8) assay in CT-26 cells. Consistent with previous studies, DMSNs at the highest concentration used here (100 µg/mL) did not show toxicity to the CT-26 cells (Fig. S6) [30–32]. Although Zn-DMSNs and DSF@DMSNs did not show substantial toxicity against CT-26 cells below 1.5 µg/mL, DSF@Zn-DMSNs remarkably suppressed cell growth (by approximately 40% at 1 µg/mL and 100% at 1.5 µg/mL, respectively) due to the production of ZnETs by the chelation of Zn²⁺ and the metabolite DTC of DSF

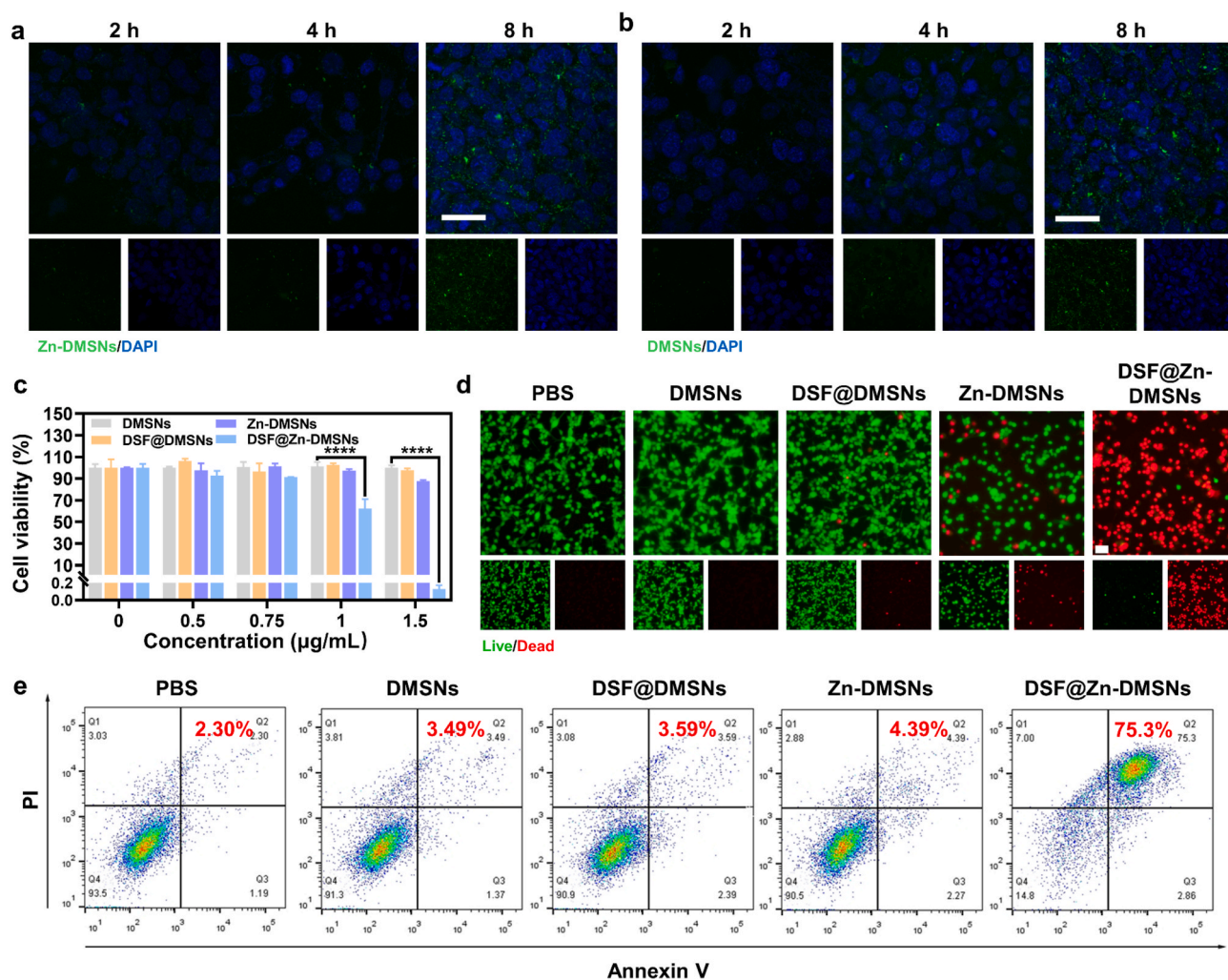


Fig. 4. *In vitro* analysis of cytotoxicity against CT-26 cancer cells. (a, b) Confocal microscope images of CT-26 cells with the cellular uptake of Zn-DMSNs (a) and DMSNs (b) for 2, 4, and 8 h (green: Zn-DMSNs labeled with FITC, blue: cell nucleus labeled with DAPI, scale bar: 50 µm). (c) The ratio of cell viability in the PBS, DMSNs, DSF@DMSNs, Zn-DMSNs, and DSF@Zn-DMSNs groups (n = 3, mean ± SD). (d) Fluorescence microscope image of CT-26 cells using dead and live staining (green: dead cells labeled with PI, red: live cells labeled with calcein-AM, scale bar: 100 µm). (e) Flow cytometry apoptosis assay stained with FITC and PI. ****, *p* < 0.0001.

(Fig. 4c and Fig. S7). To investigate the influence of the potential generation of reactive oxygen species (ROS), we then conducted an electron spin resonance (ESR) assay, a technique well suited for detecting and quantifying ROS. We incubated 10 $\mu\text{g}/\text{mL}$ DSF@Zn-DMSNs and 10 $\mu\text{g}/\text{mL}$ Zn-DMSNs with a 100 μM H_2O_2 solution for 5 min individually before performing the ESR assay. No obvious ROS generation was observed, which suggested that the cytotoxic effect of DSF@Zn-DMSNs is not due to ROS generation (Fig. S8). To better understand the safety of Zn-DMSNs nanoparticles and DSF@Zn-DMSNs nanoparticles, we

cocultured Zn-DMSNs and DSF@Zn-DMSNs with NCM460 cells (normal tissue cells) for 24 h and assessed cell viability. At a concentration of 5 $\mu\text{g}/\text{mL}$, no significant cytotoxicity was observed, suggesting that both Zn-DMSNs (Fig. S9a) and DSF@Zn-DMSNs (Fig. S9b) maintain a favorable safety profile even in the context of normal cells.

The therapeutic efficacy of DSF@Zn-DMSNs was further investigated using calcein-AM/PI staining. Live cells were stained with calcein-AM (green), and dead cells were stained with PI (red) (Fig. 4d) [33]. The green fluorescence intensity in the PBS group, DMSNs group and

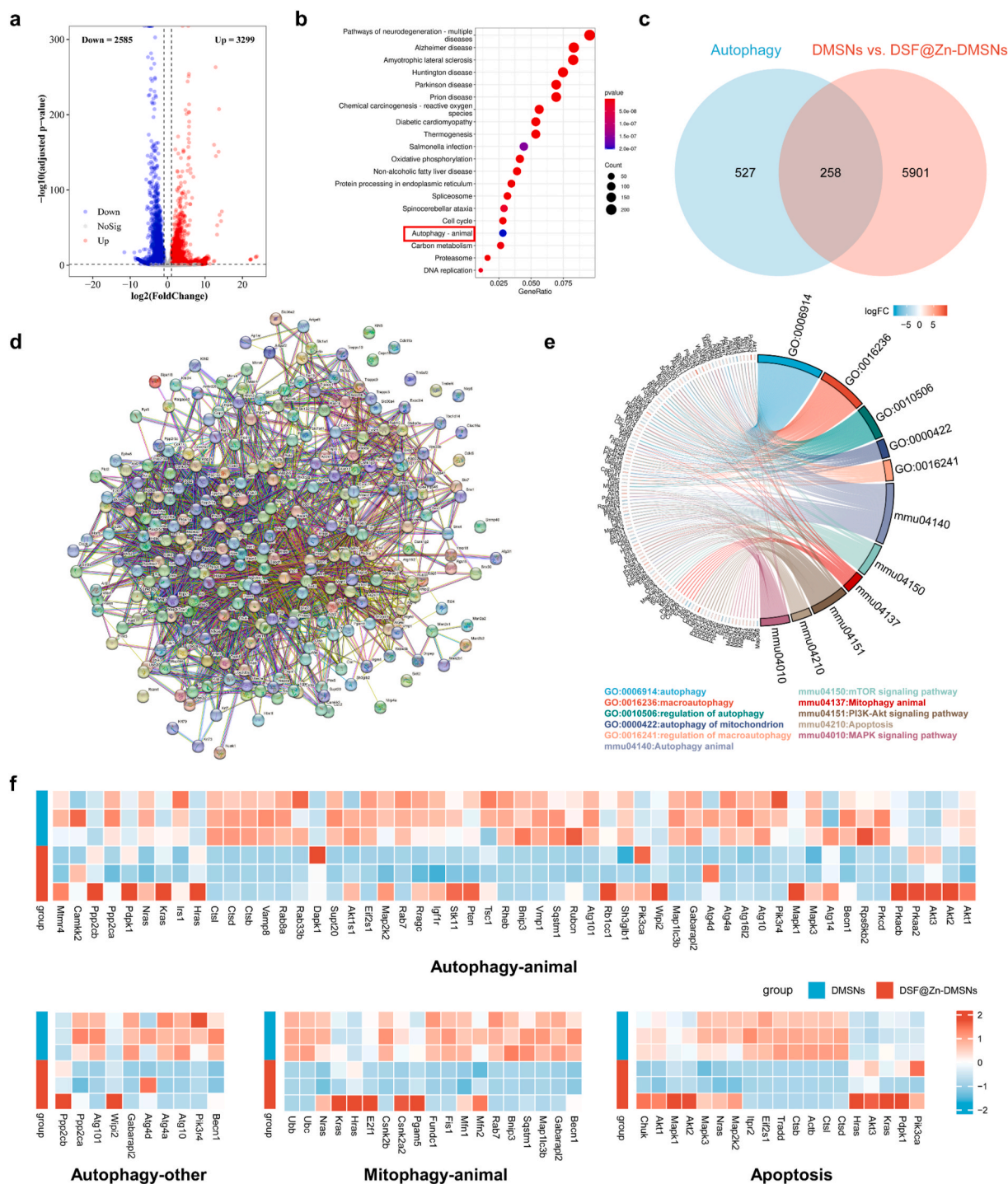


Fig. 5. mRNA sequencing analysis of CT-26 incubated with DMSNs and DSF@Zn-DMSNs. (a) Volcano map of DEGs between the DMSNs and DSF@Zn-DMSNs groups. (b) KEGG pathway enrichment analysis based on the DEGs between the DMSNs and DSF@Zn-DMSNs groups. (c) Venn diagram of 258 functional DEGs among the DEGs and autophagy. (d) PPI analysis of the 258 functional DEGs. (e) KEGG and Gene Ontology (GO) analysis based on 258 functional DEGs. (f) Heatmap analysis of the genes related to the autophagy-animal, autophagy-other, mitophagy-animal and apoptosis pathways based on 258 functional DEGs and their related Z scores.

DSF@DMSNs group was similarly strong and that in the Zn-DMSNs group and DSF@Zn-DMSNs group was significantly decreased, while strong red fluorescence intensity was observed in both the Zn-DMSNs and DSF@Zn-DMSNs groups. Notably, the DSF@Zn-DMSNs group showed the weakest green fluorescence intensity and the strongest red fluorescence intensity, indicating that DSF@Zn-DMSNs could produce the strongest cytotoxic efficacy in CT-26 cells. Flow cytometry was utilized to validate cell apoptosis using double staining with annexin V-FITC and PI (Fig. 4e). Once again, the DSF@Zn-DMSNs group showed the highest percentage of cell apoptosis among all the groups, while little cell apoptosis was observed in the DMSNs, DSF@DMSNs, and Zn-DMSNs groups. Collectively, these results confirmed that DSF@Zn-DMSNs could produce the strongest cytotoxic efficacy, possibly by the chelation reaction of Zn^{2+} and DSF to produce ZnETs.

2.4. Therapeutic mechanisms of DSF@Zn-DMSNs for autophagy activation

Encouraged by the results above, we further investigated the underlying therapeutic mechanisms of DSF@Zn-DMSNs for killing cancer cells. CT-26 cells were incubated with DSF@Zn-DMSNs at a concentration of 1.5 $\mu\text{g}/\text{ml}$, and mRNA sequencing was subsequently performed, while DMSNs were used as a control to exclude the influence of DMSNs. Based on $\text{Padj} < 0.05$ and $|\log_2(\text{fold change})| > 1$, there were 5884 significant differentially expressed genes (DEGs) between the DMSNs and DSF@Zn-DMSNs groups, among which 3299 DEGs were upregulated (Fig. S10) and 2585 DEGs were downregulated (Fig. 5a). Together with the principal component analysis (PCA) results (Fig. S11), these data indicated that DSF@Zn-DMSNs treatment significantly changed gene expression in CT-26 cells. Based on the Kyoto Encyclopedia of Genes and Genomes (KEGG) and Gene Ontology (GO) databases, further functional analysis was conducted using the sequencing results above (Fig. 5b and Fig. S12). DSF@Zn-DMSNs treatment significantly altered the genes related to the regulation of autophagy-related pathways, indicating that DSF@Zn-DMSNs upregulated autophagy in cancer cells. In addition, in gene set enrichment analysis (GSEA), a negative correlation in the glycolysis pathway was observed, indicating an overall inhibition of the glycolysis pathway in CT-26 cells after DSF@Zn-DMSNs treatment (Fig. S13), which could be attributed to the function of Zn(II) in ZnETs according to previous research [34].

We then screened for the functional DEGs according to gene sets in the autophagy database (www.tanpaku.org), and 258 functional DEGs were selected to evaluate the therapeutic efficacy of DSF@Zn-DMSNs (Fig. 5c and Table S2). Moreover, the related functional DEGs were analyzed in the protein–protein interaction network (PPI) (Fig. 5d), and the neighboring proteins connected to the leading proteins, including SQSTM1 (p62), Atg4a and Atg101, were discovered, while these genes were among the key regulatory proteins of autophagy [1,35]. Meanwhile, KEGG and GO analyses were conducted to identify the enrichment of functional DEGs, and the results further confirmed the existing changes involving in the changes in autophagy, macroautophagy, regulation of autophagy, autophagy-animal, and apoptosis pathways, suggesting that DSF@Zn-DMSNs treatment potentially functioned in the regulation of autophagy during the inhibition of colorectal cancer (Fig. 5e). Finally, the expression levels of the functional DEGs mentioned above and their related Z scores in the DMSNs group and DSF@Zn-DMSNs group were analyzed, and the results of the heatmap suggested that DSF@Zn-DMSNs significantly altered the genes related to the autophagy-animal, autophagy-other, mitophagy-animal and apoptosis pathways (Fig. 5f). These results together illustrated that the potential underlying mechanisms of DSF@Zn-DMSNs for inhibiting colorectal cancer were potentially related to the regulation of autophagy-related genes and pathways according to the results and analysis above.

2.5. Activation of autophagy by DSF@Zn-DMSNs facilitates DAMPs release

As an autophagy-related, ubiquitin-binding protein, p62 is able to directly bind to LC3II, thereby causing autophagic degradation of p62 [36]. It is convenient to study autophagic flux by measuring p62 levels under context-dependent inhibition or induction of autophagy. As an indicator of autophagy induction, Western blot assays were also used to determine LC3 turnover to detect autophagy activation [37]. Therefore, the expression of autophagy-related proteins (LC3, p62) in CT-26 cells cocultured with DMSNs, DSF@DMSNs, Zn-DMSNs or DSF@Zn-DMSNs was evaluated via Western blot assay (Fig. 6a). The results showed that the LC3II/LC3I ratio increased while the expression of p62 decreased after Zn-DMSNs or DSF@Zn-DMSNs treatment compared to DMSNs or DSF@DMSNs treatment, indicating that autophagy in CT-26 cells was activated, which could potentially be due to the effect of Zn^{2+} based on previous research (Fig. 6a).

Meanwhile, the presentation of DAMPs, including HMGB1, ATP, and CRT compounds, from dying tumor cells to APCs can be augmented by autophagy. As one of the biomarkers of necrosis, HMGB1 is usually retained in cancer cells but released to the extracellular matrix when the cell dies. CRT severed as “eat me” signals, together with extracellular HMGB1 released from the nucleus of dead cancer cells, could promote the phagocytosis, maturation and antigen presentation of dendritic cells (DCs) [5], while ATP stimulated the maturation of DC precursors for its function as a “find me” signal [38]. All these factors helped stimulate CTL infiltration into tumors. Hence, HMGB1, CRT, and ATP were measured by Western blot, immunofluorescence (IF) or enzyme-linked immunosorbent assay (ELISA) (Fig. 6b–h). Meanwhile, the Western blot results illustrated the decreased expression of intracellular HMGB1 after DSF@Zn-DMSNs treatment (Fig. 6b). ELISA was subsequently performed on the supernatants, and the results showed that ZnETs induced significantly higher HMGB1 release than Zn-DMSNs compared to the PBS group (Fig. 6c). This finding indicates that ZnETs are more effective than Zn^{2+} in promoting HMGB1 release from dying cancer cells. Furthermore, we discovered that HMGB1 release was strongly inhibited by the autophagy inhibitors 3-MA and bafilomycin A1, highlighting the crucial role of autophagy in ZnET-induced HMGB1 release during ICD (Fig. 6d). The cellular localization of HMGB1 in cancer cells was then investigated using immunofluorescence. The results revealed strong HMGB1 intensity in cancer cells for the PBS, DMSNs and DSF@DMSNs groups, while HMGB1 intensity was decreased in the Zn-DMSNs group and was scarcely observed in the DSF@Zn-DMSNs groups, indicating significant HMGB1 release caused by Zn^{2+} and ZnETs (Fig. 6g). This observation was consistent with the Western blot results. Then, the cellular ATP level was analyzed in CT-26 cells cocultured with DMSNs, DSF@DMSNs, Zn-DMSNs or DSF@Zn-DMSNs. DSF@Zn-DMSNs significantly decreased the cellular ATP concentration, suggesting that DSF@Zn-DMSNs treatment potentially promoted the secretion of ATP into the extracellular matrix (Fig. 6e). Additionally, autophagy inhibitors significantly inhibited the loss of cellular ATP (Fig. 6f), demonstrating the importance of autophagy in ATP release and subsequent ICD induction. Additionally, CRT exposure in CT-26 cells was measured through immunofluorescence. As shown in Fig. 6h, increased expression of CRT on the cancer cell surface was observed after Zn-DMSNs or DSF@Zn-DMSNs treatment, while the strongest intensity was observed in the DSF@Zn-DMSNs group, suggesting that ZnETs caused the most exposure of CRT on the surface of CT-26 cells after DSF@Zn-DMSNs treatment. Moreover, autophagy inhibitors remarkably disrupted CRT exposure in the DSF@Zn-DMSNs group, which better confirmed the function of autophagy in ZnET-induced CRT exposure and ICD induction (Fig. 6h). In summary, for the first time, we discovered that ZnETs generated *in situ* by DSF@Zn-DMSNs treatment exerted anticancer effects via autophagy amplification and DAMPs release and therefore potentially boosted the progression of ICD.

DCs are responsible for antigen-presenting characteristics, which

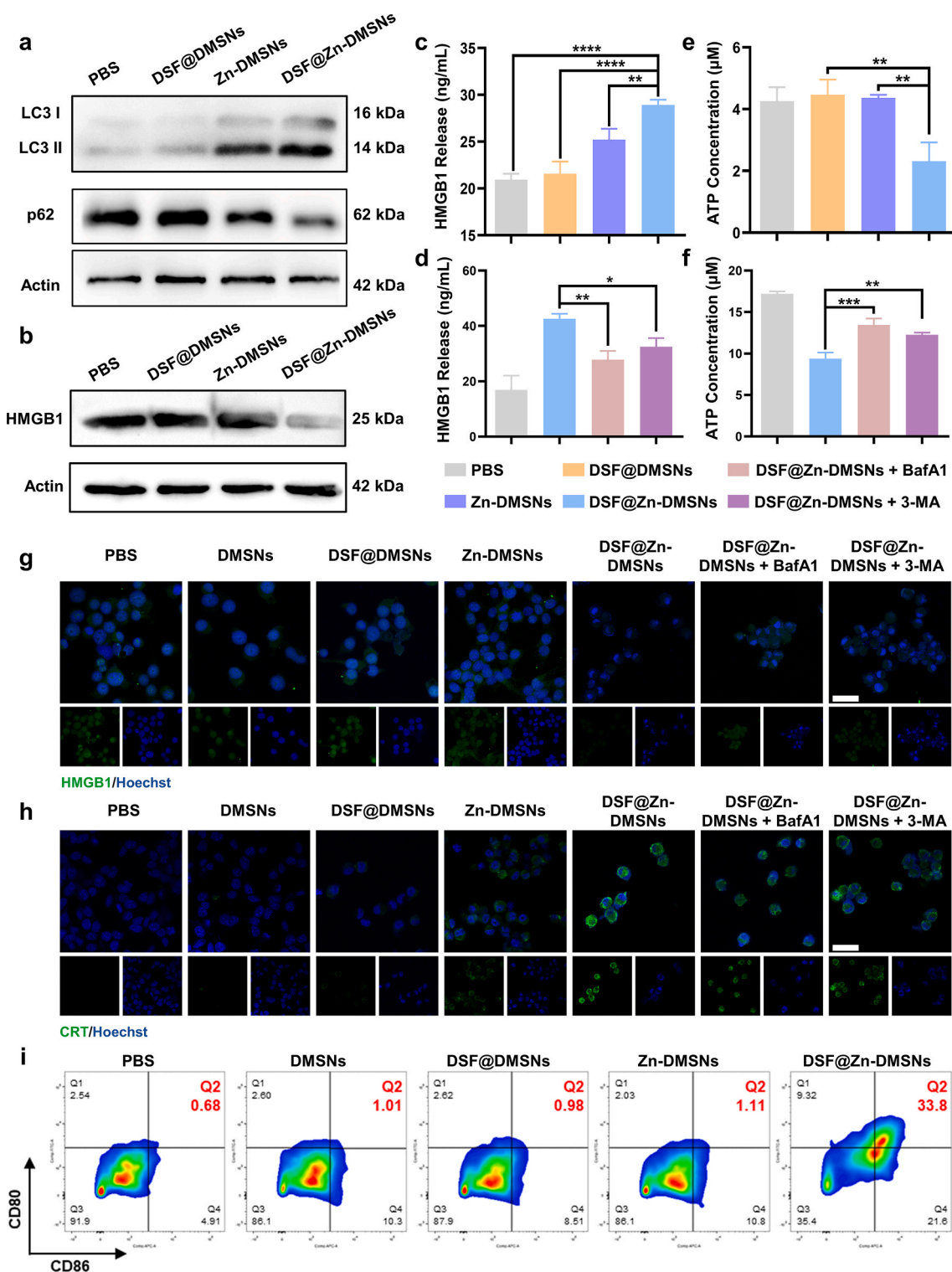


Fig. 6. *In vitro* therapeutic mechanisms of DSF@Zn-DMSNs against CT-26 cancer cells. (a) Western blot assay of LC3 and p62 expression in CT-26 cancer cells. (b) Western blot assay of HMGB1 expression in CT-26 cancer cells. (c) HMGB1 released from CT-26 cells measured by ELISA (n = 3, mean ± SD). (d) DSF@Zn-DMSNs induced HMGB1 release in the presence or absence of the autophagy inhibitors BafA1 and 3-MA, as determined by ELISA (n = 3, mean ± SD). (e) Intracellular ATP expression of CT-26 cells measured by ATP assay kits (n = 3, mean ± SD). (f) DSF@Zn-DMSNs induced CT-26 cell release in the presence or absence of the autophagy inhibitor BafA1 and 3-MA treatment, as determined by ATP assay kits (n = 3, mean ± SD). (g) Immunofluorescence examination of HMGB1 release in CT-26 cells during different treatments and in the presence or absence of autophagy inhibitor BafA1 and 3-MA treatment (green: HMGB1 labeled with FITC, blue: cell nucleus labeled with Hoechst, scale bar: 20 μm). (h) Immunofluorescence examination of CRT exposure in CT-26 cells under different treatments and in the presence or absence of the autophagy inhibitors BafA1 and 3-MA (scale bar: 50 μm). (i) Flow cytometric results of DCs stained with anti-CD11c PE, anti-CD80 FITC, and anti-CD86 APC for maturation identification. *, p < 0.05; **, p < 0.01; ***, p < 0.001; ****, p < 0.0001.

activate naive T cells, playing a key role in both innate and adaptive immunity [39]. In response to antigen exposure, immature DCs engulf antigens and present them as peptides in nearby lymph nodes as they migrate. As a result, immature DCs undergo maturation and present the complex peptide to naive T cells, which stimulates their differentiation [40]. To investigate the activation of immature DCs by released DAMPs from tumor cells induced by nanoparticles, flow cytometry was used to detect upregulation of the costimulatory molecules CD80/CD86 in bone marrow-derived DCs (BMDCs). BMDCs were cocultured with the supernatant of CT-26 cells cocultured with assigned nanoparticles for 24 h before flow cytometry analysis was carried out. The results showed that compared to the other four groups, the DSF@Zn-DMSNs group had the highest CD80⁺CD86⁺ population (Fig. 6i), indicating that the DAMPs released by DSF@Zn-DMSNs could stimulate DC maturation and therefore potentially boost the progression of ICD.

2.6. *In vivo* therapeutic effect of DSF@Zn-DMSNs

Encouraged by the remarkable autophagy augmentation and ICD promotion efficiency for ZnETs generated by DSF@Zn-DMSNs treatment in cancer cells, we evaluated the antitumor effect on BALB/c mice bearing CT-26 cancer cells. The CT-26-bearing mice were randomly divided into five groups: (a) PBS, (b) DMSNs, (c) DSF@DMSNs, (d) Zn-DMSNs, and (e) DSF@Zn-DMSNs ($n = 6$ in each group). Mice were injected with assigned treatments twice before they were sacrificed, and the anticancer efficiency over two consecutive weeks was analyzed (Fig. 7a). Compared to the PBS group, DMSNs group and DSF@DMSNs group, although Zn-DMSNs inhibited tumor growth to some extent, DSF@Zn-DMSNs produced the best therapeutic efficiency (inhibition rate 83.1%, $p < 0.0001$) (Fig. 7b and c), indicating that the antitumor performance of ZnETs generated *in situ* by TME-responsive DSF@Zn-DMSNs surpassed that of Zn²⁺ or DSF alone *in vivo*. After fourteen days of monitoring, this efficiency was confirmed by comparing the volume and weight of dissected tumor tissues (Fig. 7d and e). The relative expression of key immune-related cytokines, such as IL6, TNF α , and IFN γ , in tumor tissues can provide more profound insights into the immunomodulatory effects of nanoparticles. The results of real-time fluorescent quantitative PCR indicated that compared to the other four groups, the relative expression of IL6, TNF α , and IFN γ was significantly increased in the DSF@Zn-DMSNs group (Fig. 7f–h), indicating the satisfactory immunomodulatory effects of DSF@Zn-DMSNs nanoparticles. Representative images of tumors in each group were taken and are shown in Fig. S14, which further proved the therapeutic efficacy of DSF@Zn-DMSNs. Collectively, the *in vivo* results confirmed the superior therapeutic efficacy of DSF@Zn-DMSNs in tumor therapy.

To further understand the therapeutic mechanism of DSF@Zn-DMSNs, harvested tumor tissue sections were fixed and processed for hematoxylin-eosin (H&E) staining, immunohistochemistry (IHC) staining for terminal deoxynucleotidyl transferase dUTP nick end labeling (TUNEL) and Ki-67, and IF staining for LC3, HMGB1, CRT, CD4 and CD8 (Fig. 7i). For H&E staining, significant nuclear polymorphism and hypercellularity were observed in the PBS group and DMSNs group, while obvious cell swelling and nuclear pyknosis were observed in the DSF@Zn-DMSNs group compared to the other four groups (Fig. 7i, 1st column). In addition, the low expression level of TUNEL and high expression level of Ki-67 further demonstrated low necrosis and high proliferation in the PBS group and DMSNs group. The increased expression level of TUNEL and decreased expression level of Ki-67 in the DSF@DMSNs group and Zn-DMSNs group illustrated the slight therapeutic efficiency of both treatments, while the highest expression level of TUNEL and lowest expression level of Ki-67 in the DSF@Zn-DMSNs group demonstrated widespread necrosis and inhibition of cell proliferation in the tumors, indicating the superior therapeutic outcomes of DSF@Zn-DMSNs compared to other treatments (Fig. 7i, the 2nd and 3rd columns). Furthermore, *in vivo* autophagy was evaluated through IF staining of LC3. Rare green fluorescence intensity was observed in the

PBS and DMSNs groups, while increasing green fluorescence intensity was observed in the DSF-DMSNs and Zn-DMSNs groups, indicating the activation of autophagy by the DSF@DMSNs and Zn-DMSNs treatments. The highest fluorescence intensity in the DSF@Zn-DMSNs group suggested an augmented autophagy effect for DSF@Zn-DMSNs nanoparticles, which was in line with the *in vitro* results (Fig. 7i, 4th column). As we have demonstrated that extracellular DAMPs were increased by amplified autophagy in DSF@Zn-DMSNs treatment *in vitro*, we further performed IF staining of HMGB1 and CRT to evaluate the release of DAMPs *in vivo*. For HMGB1 staining, strong fluorescence intensity was observed in the PBS group, DMSNs group, and DSF@DMSNs group, while weak fluorescence intensity was observed in the Zn-DMSNs group and DSF@Zn-DMSNs group, indicating the promotion of HMGB1 release induced by Zn-DMSNs and DSF@Zn-DMSNs treatment (Fig. 7i, 5th column). Regarding the results of CRT staining, rare fluorescence intensity was observed in the PBS group, DMSNs group, and DSF@DMSNs group, while strong fluorescence intensity was observed in the Zn-DMSNs group and DSF@Zn-DMSNs group, indicating the promotion of CRT exposure induced by Zn-DMSNs and DSF@Zn-DMSNs treatment. The results above together indicated that the extracellular DAMPs were increased by amplified autophagy in DSF@Zn-DMSNs treatment (Fig. 7i, the 6th column). Then, tumor sections were stained with CD4 and CD8 to determine whether the infiltration of T cells in tumors was enhanced (Fig. 7i, 7th and 8th columns). Although slightly increased CD4⁺ T cells were observed, the strongest red fluorescence intensity for CD8 showed significant upregulation of CD8⁺ T cell infiltration in the DSF@Zn-DMSNs group, which further proved that ZnETs generated by *in situ* reaction remarkably promoted the stimulation of CTL infiltration and subsequent ICD after DSF@Zn-DMSNs treatment (Fig. 7i and Fig. S15). All the experimental evidence collectively confirmed the excellent antitumor efficacy of DSF@Zn-DMSNs through ion-chelation therapy and autophagy-amplified ICD in colorectal cancer treatment. Finally, the biocompatibility of DSF@Zn-DMSNs was investigated *in vivo*. Compared to the PBS group, no significant difference in body weight loss was observed after different treatments (Fig. S16). Simultaneously, H&E staining of the major organs, including the heart, liver, spleen, lung and kidney, showed no obvious histologic damage in the different groups at the end of the experiment (Fig. S17). Similarly, the results of routine blood tests and blood biochemical indicators of all groups were in the normal range, and there were no significant differences among all groups, which demonstrated the safety of the nanoparticles (Fig. S18). Therefore, all of the above results revealed that at the administered dosage, DSF@Zn-DMSNs exerted satisfactory therapeutic efficacy with almost no acute toxicity. Finally, we studied the biodistribution of the DSF@Zn-DMSNs. To evaluate this, we labeled DSF@Zn-DMSNs with Cy5.5, a near-infrared fluorescent dye, and administered these labeled nanoparticles intratumorally. By performing bioimaging at various time points up to 72 h postinjection ($n = 3$ at each time point), we were able to track the distribution of the nanomedicine. The signal decreased from the 24-h mark on, and by the 72-h mark, there was almost no signal detectable at the tumor site, implying that the majority of the nanomedicine had been degraded or cleared from the body (Fig. S19). It is worth noting that almost no signal could be observed in additional studies examining nanoparticle distribution in other tissues (such as heart, liver, kidney, spleen, lung), providing a more comprehensive understanding of the biodistribution of DSF@Zn-DMSNs.

We then evaluated distant antitumor immunity using a bilateral subcutaneous tumor model. The design and schedule of the experiment are shown in Fig. 8a. We inoculated the primary tumor xenograft into the right abdomen as the primary tumor. After the primary tumor volume reached approximately 100 mm³, another tumor xenograft was placed in the left abdomen to create an artificial metastatic tumor on the left side. Mice were randomly divided into five groups: (a) PBS, (b) DMSNs, (c) DSF@DMSNs, (d) Zn-DMSNs, and (e) DSF@Zn-DMSNs ($n = 5$ in each group). Mice were injected with assigned treatments at day 1 and day 7 with the same dose as previously described, and the

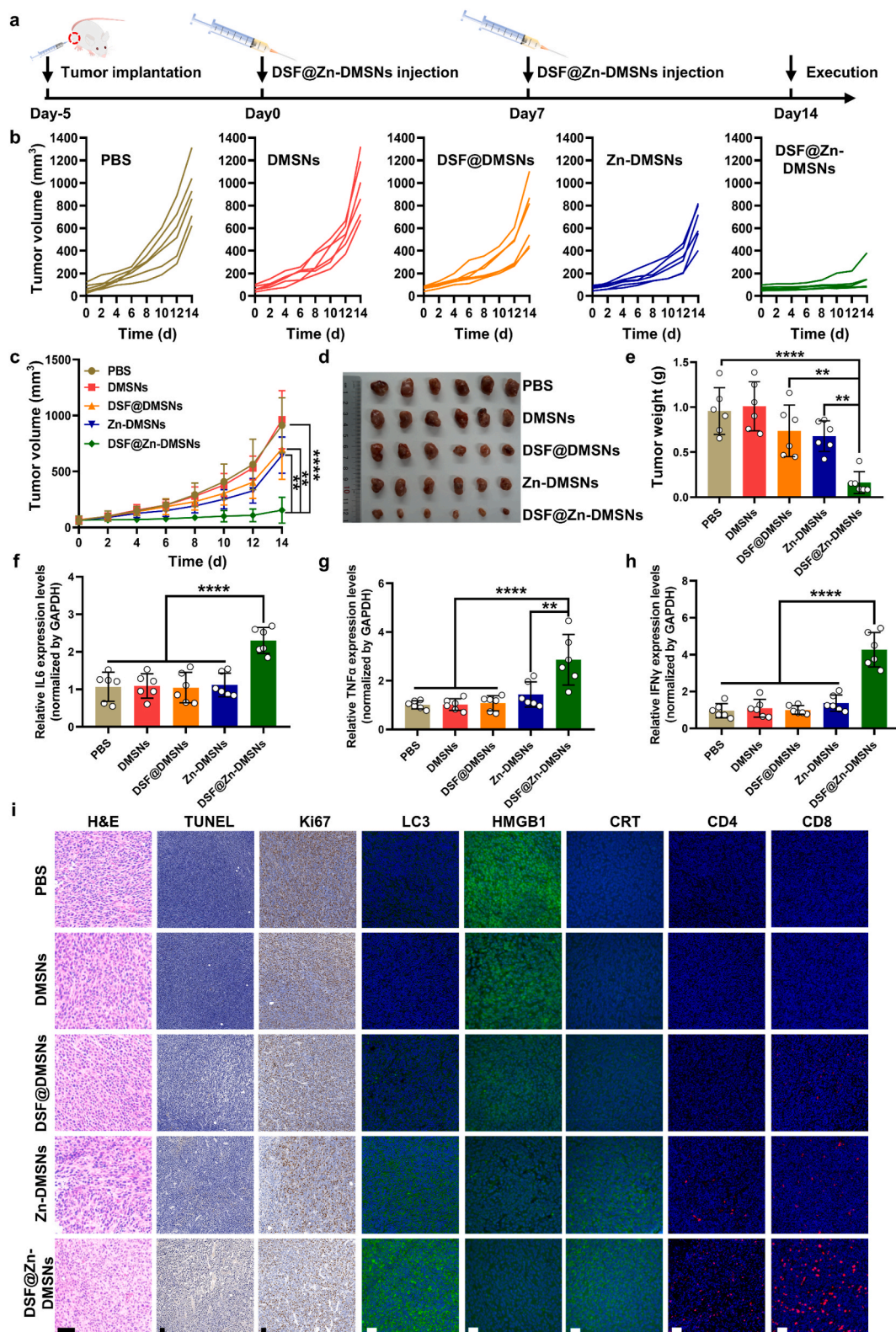


Fig. 7. *In vivo* therapeutic effect of DSF@Zn-DMSNs. (a) Schematic diagram of constructing the subcutaneous tumor model and two-week treatment options. (b) Tumor growth curves of each mouse in the PBS, DMSNs, DSF@DMSNs, Zn-DMSNs, and DSF@Zn-DMSNs groups. (c) Tumor volume curves in different groups (n = 6, mean ± SD). (d) Digital images of dissected tumor tissues (n = 6). (e) The weight of dissected tumor tissues (n = 6, mean ± SD). (f–h) qPCR results of immune-related cytokines, including IL6 (f), TNFα (g), and IFNγ (h), in tumor tissues. (i) Immunohistochemical (H&E, Ki67 and TUNEL) and immunofluorescence analyses (LC3, HMGB1, CRT, CD4, and CD8) of tumor tissue sections in different groups (scale bar: 50 μm). **, p < 0.01, ****, p < 0.0001.

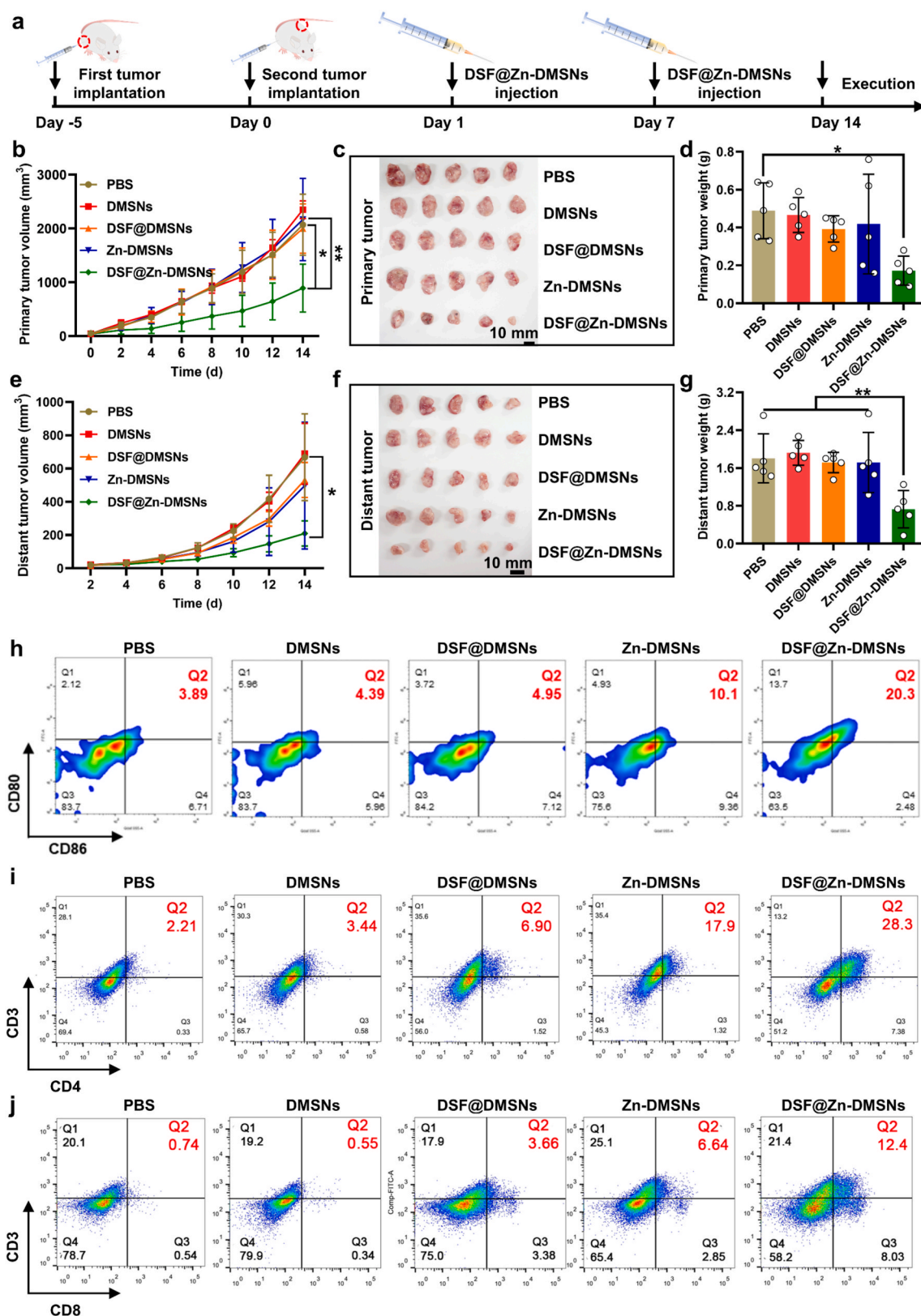


Fig. 8. *In vivo* antitumor and immunotherapy investigation in a bilateral subcutaneous xenograft model. (a) Schematic diagram of constructing the bilateral subcutaneous xenograft tumor model and two-week treatment options. (b–d) Primary tumor volume curves (b), dissected primary tumor tissues (c), and primary tumor weight (d) in different groups (n = 5, mean ± SD). (e–g) Distant tumor volume curves (e), dissected distant tumor tissues (f), and distant tumor weight (g) in different groups (n = 5, mean ± SD). (h) Flow cytometric results of DCs in primary tumors stained with anti-CD45 Pacific blue, anti-CD11c PE, anti-CD80 FITC, and anti-CD86 BV650 for maturation identification. (i) Flow cytometric results of the CD3⁺CD4⁺ T cells in primary tumors stained with anti-CD45 Pacific blue, anti-CD3 FITC, and anti-CD4 APC for identification. (j) Flow cytometric results of the CD3⁺CD8⁺ T cells in primary tumors stained with anti-CD45 Pacific blue, anti-CD3 FITC, and anti-CD8 APC/Fire 750 for identification. *, p < 0.05; **, p < 0.01.

anticancer efficiency was analyzed. Treatment results of different nanoparticles against the primary tumor (Fig. 8b–d) and mimetic distant tumors were obtained (Fig. 8e–g). Administration of DMSNs showed no obvious therapeutic effect on either primary tumors or distant tumors. Compared to the PBS group, DMSNs group and DSF@DMSNs group, although DSF@DMSNs and Zn-DMSNs nanoparticles inhibited the growth of both primary tumors and distant tumors to some extent, DSF@Zn-DMSNs produced the best therapeutic efficiency (primary tumor: inhibition rate 56.9%, $p = 0.0139$; distant tumor: inhibition rate 68.6%, $p = 0.0433$), indicating the antitumor performance of ZnETs generated *in situ* by TME-responsive DSF@Zn-DMSNs, as well as augmenting the systemic antitumor immune response *in vivo*.

To investigate the underlying mechanism of the antitumor immune responses *in vivo*, both primary tumors and distant tumors were harvested and digested into single-cell samples before DC maturation markers (CD80/CD86) and T cell infiltration (CD3/CD4 and CD3/CD8) were investigated through flow cytometry (Fig. 8h–j, Fig. S20a–c). The results showed that the proportions of CD80/CD86-positive cells in primary tumors in the PBS group, DMSNs group, DSF@DMSNs group, Zn-DMSNs group, and DSF@Zn-DMSNs group were 3.89%, 4.39%, 4.95%, 10.1%, and 20.3%, respectively (Fig. 8h). The counterparts in distant tumors were 3.69%, 2.12%, 4.03%, 10.4%, and 20.1%, respectively (Fig. S20a). These results together indicated that DCs could be activated by autophagy, while DSF@Zn-DMSNs could significantly enhance the activation level due to the synergy of DAMPs release and autophagy. The quantity of helper T cells labeled by CD3⁺CD4⁺ was increased in the primary tumor of the DSF@Zn-DMSNs group (Fig. 8i), while such tendency was also observed in the distant tumor (Fig. S20b). Additionally, the quantity of cytotoxic T cells labeled by CD3⁺CD8⁺ was markedly increased in the primary tumor (Fig. 8j) and distant tumor (Fig. S20c) after DSF@Zn-DMSNs treatment. The results of flow cytometry together illustrated that ZnETs generated by *in situ* chelation reactions could promote DC maturation and stimulate ICD, thereby enhancing chemoimmunotherapy in cancer treatment.

3. Conclusion

In this work, a TME-responsive DSF@Zn-DMSNs nanoplatform that could simultaneously deliver Zn²⁺ and DSF into cancer cells was designed and engineered for *in situ* ZnET generation, autophagy amplification, and ICD. The pH-sensitive DSF@Zn-DMSNs could corelease Zn²⁺ and DSF under mildly acidic tumor conditions and spontaneously generate highly toxic ZnETs via an *in situ* chelation reaction, resulting in tumor cell death. Furthermore, for the first time, we revealed that ZnETs with strong autophagy amplification ability, including the upregulation of LC3 and downregulation of p62, remarkably promoted the extracellular release of DAMPs, represented by HMGB1, CRT and ATP, which further stimulated the maturation and antigen presentation of DCs and therefore facilitated T cell infiltration to achieve maximum therapeutic efficacy in colorectal cancer treatment. The *in vivo* results confirmed the superior therapeutic efficacy of DSF@Zn-DMSNs in tumor therapy with a high inhibition rate. This study provides a smart *in situ* chelation strategy with TME-responsive autophagy amplification to augment DAMPs release, thus boosting tumor chemoimmunotherapy with satisfactory biosafety.

4. Materials and methods

4.1. Materials

Hexadecyl trimethyl ammonium bromide (CTAB) (Cat. No. 57-09-0), Trolamine (TEA) (Cat. No. 102-71-6) and Triton X-100 (Cat. No. 9002-93-1) were purchased from Yien Chemical Technology Co., Ltd. (Shanghai, China). Sodium salicylate (NaSal) (Cat. No. S817536) and ammonia solution (NH₃·H₂O) (Cat. No. A801009) were purchased from Macklin Biochemical Co., Ltd. (Shanghai, China). Tetraethyl

orthosilicate (TEOS) (Cat. No. T110593) was purchased from Aladdin Biochemical Technology Co., Ltd. (Shanghai, China). Hydrochloric acid (HCl) (Cat. No. 10011018) was purchased from Sinopharm Chemical Reagent Co., Ltd. (Shanghai, China). Zinc nitrate hexahydrate (Zn(NO₃)₂·6H₂O) (Cat. No. 10196-18-6), collagenase from clostridium histolyticum (Cat. No. 9001-12-1) and deoxyribonuclease I from bovine pancreas (Cat. No. 9003-98-9) were purchased from Sigma–Aldrich Trading Co., Ltd. (Shanghai, China). Ethanol (Cat. No. 64-17-5) and methanol (Cat. No. 67-56-1) were purchased from Lingfeng Chemical Reagent Co., Ltd. (Shanghai, China). Disulfiram (DSF) (Cat. No. T0054) was purchased from Topscience Co., Ltd. (Shanghai, China). Dulbecco's modified Eagle medium (DMEM) (Cat. No. C11995500BT) and fetal bovine serum (FBS) (Cat. No. 10099) were purchased from Gibco (California, USA). 4,6-Diamidino-2-phenylindole (DAPI) (Cat. No. C1006), calcein-AM/PI cell viability/cytotoxicity assay kit (Cat. No. C2015 M), ATP assay kit (Cat. No. S0026) and annexin V-FITC apoptosis assay kit (Cat. No. C1062L) were purchased from Beyotime Biotechnology Co., Ltd. (Shanghai, China). Calreticulin (CRT) polyclonal antibody (Cat. No. 27298-1-AP) and HMGB1 antibody (Cat. No. 10829-1-AP) were purchased from Proteintech Biotechnology Co., Ltd. (Haimen, China). p62/SQSTM1 antibody (Cat. No. T55546) was purchased from Abmart Inc. (Shanghai, China). LC3 antibody (Cat. No. 4108) was purchased from Cell Signaling Technology Co., Ltd. (Massachusetts, USA). ELISA kit for HMGB-1 analysis (Cat. No. RX203303 M) was purchased from Ruixin Technology Co., Ltd. (Quanzhou, China). Granulocyte-macrophage colony-stimulating factor (GM-CSF) (Cat. No. abs04720) and recombinant mouse interleukin-4 (IL-4) (Cat. No. abs04697) were purchased from Absin Technology Co., Ltd. (Beijing, China). Anti-CD11c PE (Cat. No. 557401), anti-CD80 FITC (Cat. No. 561954), anti-CD86 APC (Cat. No. 558703), anti-CD86 BV650 (Cat. No. 564200), anti-CD45 Pacific blue (Cat. No. 558108), anti-CD3 FITC (Cat. No. 561801) and anti-CD4 APC (Cat. No. 561091) were purchased from BD Pharmingen Co., Ltd. (New Jersey, USA). anti-CD8 APC/Fire 750 (Cat. No. 344745) was purchased from Biolegend Co., Ltd. (California, USA).

4.2. Cell lines and animals

Murine CT-26 colorectal cancer cells were purchased from Shanghai Cell Bank, Chinese Academy of Sciences (Shanghai, China). CT-26 cells were maintained in DMEM complete medium containing 10% FBS and incubated at 37 °C with 5% CO₂. BALB/c mice (6 weeks, male) were purchased from Shanghai Slac Laboratory Animal Co. Ltd. (Shanghai, China) and were reared in the Center for Medical Science and Innovation of the Shanghai Tenth People's Hospital (Shanghai, China). The animal study was approved by the Ethics Committee on Animals of Shanghai Tenth People's Hospital (approval number: SHDSYY-2022-KR0104). The animals used in laboratory experiments were kept in an environment free from specific pathogens. During the experiments, mice were raised using temperature-controlled rooms (20–24 °C) with relative humidity between 50 and 60% and a 12-h light/dark cycle.

4.3. Synthesis of dendritic mesoporous silica nanoparticles (DMSNs)

DMSNs were synthesized using an achievable anion-assisted process as previously reported [41]. CTAB (1.535 g) and TEA (0.347 g) were added to 100 mL deionized water and stirred at a speed of 400 rpm at 80 °C for 1 h. Then, with dropwise additions of 10 mL TEOS, the mixture was stirred at a speed of 400 rpm for 2 h. The samples were centrifuged at 15000 rpm for 5 min to collect the products. All remaining reactants were washed repeatedly with ethanol and deionized water. Refluxing the products with HCl (37 wt%)/ethanol (ratio 1:9) at 60 °C for 12 h three times removed CTAB from the products. The final products, DMSNs, were lyophilized to obtain nanoparticle powders.

4.4. Synthesis of Zn²⁺-doped DMSNs (Zn-DMSNs)

We followed a hydrothermal process as previously reported for the preparation of Zn-DMSNs [21], but an opportune alteration was made. First, in deionized water, DMSNs (65 mg) synthesized in the previous step and Zn(NO₃)₂·6H₂O (208 mg) were dissolved and mixed with magnetic stirring, and then NH₃·H₂O (30 wt %, 6 mL) was added dropwise. We transferred the mixture into a 100 mL Teflon autoclave. During 10 h of heating at 140 °C, the reaction was conducted. After the Teflon autoclave was fully cooled, we centrifuged the white products at 15,000 rpm for 5 min and then removed the residues by washing alternately with ethanol and deionized water three times. To improve the dispersibility of the nanoparticles, Zn-DMSNs (10 mg) were mixed with mPEG-silane (50 mg) in an ethanol solution (100 mL) and stirred at 300 rpm for 24 h at a reaction temperature of 60 °C.

4.5. Preparation of DSF@Zn-DMSNs

Magnetic stirring was used for 12 h to disperse PEGylated Zn-DMSNs (20 mg) and DSF (80 mg) in an ethanol solution (10 mL). To remove the free DSF, the products were centrifuged (at 15,000 rpm for 5 min) followed by a wash using ethanol and deionized water. To track the distribution of nanoparticles, these nanoparticles were mixed with mPEG-silane and amino-PEG-silane at a ratio of 1:1. Then, DMSNs and Zn-DMSNs were labeled with FITC, and DSF@Zn-DMSNs were labeled with Cy5.5 carboxylic acid for further experiments.

4.6. Characterization of nanoparticles

Transmission electron microscopy (TEM) images were observed by an FEI Tecnai G2 F20 field-emission transmission electron microscope (FEI, Oregon, USA). The morphology of the nanoparticles was acquired using a Magellan 400 field-emission scanning electron microscope (FEI, Oregon, USA). The size and zeta potential of the nanoparticles were measured in deionized water with dynamic light scattering (DLS) using a Nano ZS90 zetasizer (Malvern Panalytical, Shanghai, China). X-ray photoelectron spectroscopy (XPS) spectra were observed to analyze the valence of the zinc component of Zn-DMSNs by a Thermo Scientific ESCALAB Xi⁺ instrument (Thermo Fisher, Massachusetts, USA). Analyses of quantitative elemental composition were performed on an Agilent 720 ES (OES) with inductively coupled plasma and optical emission spectrometry (Agilent, California, USA).

4.7. In vitro DSF@Zn-DMSNs biodegradation

To further investigate the disintegration of nanoparticles in simulated body fluids (SBFs) at different pH levels, Zn-DMSNs were dissolved in SBF solutions at pH 6.5 and pH 7.4 with mild magnetic agitation (200 rpm). A 1.5 mL sample was taken from the test solution at each time point (2, 4, 8, 12, 24 and 48 h) and centrifuged to obtain its supernatant and precipitate. The contents of Zn and Si in the supernatant were measured by ICP-OES. TEM images were captured for the remaining nanoparticles to assess their structural changes.

4.8. In vitro cellular uptake

To examine the cellular uptake of DMSNs and Zn-DMSNs, 5 × 10⁵ CT-26 cells were seeded into 6-well plates with 2 mL of DMEM complete medium for 24 h and then incubated with FITC-labeled nanoparticles at a concentration of 1.5 µg/mL for 2 h, 4 h and 8 h. Next, the cells were fixed with 4% paraformaldehyde (POM) and stained with DAPI. Fluorescence graphs at different time points were acquired by TS2R-FL fluorescence inversion microscopy (Nikon, Tokyo, Japan).

4.9. In vitro safety experiment

Colorectal cancer cells CT-26 and intestinal epithelial cells NCM-460 were used to test the biological security of Zn-DMSNs and DSF@Zn-DMSNs. A total of 5 × 10⁵ CT-26 cells and NCM-460 cells were seeded into 96-well plates with 100 µL of DMEM complete medium for 24 h, and different concentrations of Zn-DMSNs and DSF@Zn-DMSNs were incubated with the cells for 24 h. CCK8/DMEM solution at a 1:9 ratio was added to each well, and the 96-well plates were incubated in a CO₂ incubator for 30 min. Then, an ELx800 microplate reader (Bio-Tek, Vermont, USA) was used to measure the absorbance per well at 450 nm.

4.10. In vitro cytotoxicity assay

The CCK8 assay was used to quantify cell viability after different treatments. A total of 3 × 10³ CT-26 cells were plated in 96-well plates with 100 µL DMEM complete medium per well. DMSNs, DSF@DMSNs, Zn-DMSNs and DSF@Zn-DMSNs at different concentrations (0, 0.5, 0.75, 1, and 1.5 µg/mL) were incubated with CT-26 cells for 24 h. The CCK8 kit was used to detect cell viability, and an ELx800 microplate reader was used to measure the absorbance at 450 nm.

4.11. Live/dead cell staining assay

Live and dead cells were observed using a calcein-AM/PI cell viability/cytotoxicity assay kit and a fluorescence microscope, and 5 × 10⁵ CT-26 cells were seeded into 6-well plates with 2 mL DMEM complete medium per well. CT-26 cells were incubated with PBS, DMSNs, DSF@DMSNs, Zn-DMSNs and DSF@Zn-DMSNs at a concentration of 1.5 µg/mL for 24 h. After removing the culture medium and washing with PBS, live cells were stained with green calcein-AM fluorescence, and dead cells were stained with red PI fluorescence for 15 min. The staining solution was removed, and the plates were washed with PBS three times. Next, TS2R-FL fluorescence inversion microscopy (Nikon, Tokyo, Japan) was used to observe and take pictures.

4.12. Flow cytometric analysis of apoptosis

An annexin V-FITC apoptosis assay kit performing FITC/PI double staining was used for apoptosis analysis. CT-26 cells (5 × 10⁵) were seeded into 6-well plates and incubated with PBS, DMSNs, DSF@DMSNs, Zn-DMSNs and DSF@Zn-DMSNs (1.5 µg/mL) for 24 h. The cells were harvested with trypsin without EDTA and resuspended in binding buffer after washing with PBS twice. Then, PI and annexin V-FITC were used to stain cells for 15 min in the dark. Then, the stained cells were tested by flow cytometry (BD Fortessa, New Jersey, USA).

4.13. mRNA sequencing analysis

mRNA sequencing was used to perform transcriptome analysis. CT-26 cells were cultured in 6-well plates at 5 × 10⁵ cells per well for 24 h and then incubated with DMSNs or DSF@Zn-DMSNs individually at a concentration of 1.5 µg/mL for 24 h. RNA was extracted by the TRIzol method. The step was carried out on ice. The enriched mRNA was reverse transcribed into double-stranded cDNA. After purification, the library was constructed, and quality detection was carried out. PE150 was used for sequencing. R.3.6.3 was used for data analysis.

4.14. Protein expression detected by western blot

The expression of LC3, p62 and HMGB1 in CT-26 cells was measured by western blot [42]. A total of 5 × 10⁵ CT-26 cells were seeded into each well of 6-well plates, incubated with 2 mL of DMEM complete medium for 24 h and lysed by RIPA buffer after incubation with PBS, DSF@DMSNs, Zn-DMSNs and DSF@Zn-DMSNs (1.5 µg/mL) for 24 h. The BCA protein assay was first used to measure the total protein

concentration of the cell lysates. Next, 20–30 µg of protein was loaded on SDS–PAGE gels and transferred to PVDF membranes. Then, the PVDF membranes were incubated with HMGB1 antibody, p62/SQSTM1 antibody and LC3 antibody. Incubating the corresponding HRP-conjugated secondary antibody was the next step. Finally, the PVDF membranes were observed by a chemiluminescence imaging system (Tanon, Shanghai, China).

4.15. *In vitro* quantitative analysis of ATP concentration and HMGB1 release

ATP assay kits were used to measure intracellular ATP concentrations. Hence, 5×10^5 CT-26 cells were seeded into 6-well plates with 2 mL DMEM complete medium per well for 24 h and treated with PBS, DSF@DMSNs, Zn-DMSNs, DSF@Zn-DMSNs, DSF@Zn-DMSNs + 3-MA and DSF@Zn-DMSNs + BafA1 (1.5 µg/mL) for 24 h. The cell culture medium was collected for HMGB1 quantification using an HMGB1 ELISA kit. The remaining tumor cells were washed with PBS and split by ATP lysate before the cellular ATP concentration was measured with an ATP assay kit.

4.16. *In vitro* evaluation of ICD

Immunofluorescence detection showed the expression of CRT and HMGB1. CT-26 cells (5×10^5) were seeded into a 6-well plate with 2 mL of DMEM complete medium per well for 24 h and incubated with PBS, DMSNs, DSF@DMSNs, Zn-DMSNs, DSF@Zn-DMSNs, DSF@Zn-DMSNs + 3-MA and DSF@Zn-DMSNs + BafA1 for 24 h. The cells were fixed with 4% paraformaldehyde, permeabilized with 0.1% Triton X-100 (except for the examination of proteins expressed on the cell membrane) and blocked with blocking solution. The cells were incubated with CRT polyclonal antibody or HMGB1 antibody overnight and then incubated with corallite488-conjugated secondary antibody for 1 h. The cell nucleus was stained with Hoechst for 5 min and observed by fluorescence inversion microscopy.

4.17. *In vitro* DC maturation experiment

According to an existing integrated method, a bone marrow cell suspension was obtained by washing the marrow cavity of BALB/c mouse legs, and then bone marrow dendritic cells (BMDCs) were obtained after density gradient centrifugation. BMDCs were cultured in RPMI 1640 complete medium with 10% FBS and were induced to differentiate into immature DCs by granulocyte-macrophage colony-stimulating factor (GM-CSF, 20 ng/mL) and interleukin-4 (IL-4, 10 ng/mL). CT-26 cells (5×10^5) were seeded into a 6-well plate with 2 mL of DMEM complete medium per well for 24 h and incubated with PBS, DMSNs, DSF@DMSNs, Zn-DMSNs and DSF@Zn-DMSNs at a concentration of 1.5 µg/mL for 24 h. Then, the supernatants of CT-26 cells were collected, and the cell debris was removed. DCs were plated in 12-well plates at 2 mL per well and cocultured with the supernatant mentioned above for 24 h. DC cells were collected and stained with anti-CD11c PE, anti-CD80 FITC and anti-CD86 APC before they were tested and analyzed.

4.18. *In vivo* biodistribution

To investigate the distribution and metabolism of nanoparticles after intratumoral injection, Cy5.5-labeled DSF@Zn-DMSNs at a dose of 2 mg/kg were injected into the tumors of tumor-bearing BALB/c mice. At 0, 2, 4, 8, 12, 24, 48 and 72 h, the mice were sacrificed, and the tumor and major organs (heart, liver, spleen, lung and kidney) were collected for fluorescence imaging using VISQUE InVivo Elite (Vieworks, Republic of Korea).

4.19. *In vivo* antitumor efficacy

To establish the tumor-bearing BALB/c mouse model, CT-26 cells during logarithmic phase were harvested after centrifugation and redispersed in normal saline at a density of $1 \times 10^6/100 \mu\text{L}$. A 100 µL cell suspension was implanted subcutaneously into the left leg of healthy male BALB/c mice (6 weeks). When the tumor volume grew to approximately 100 mm³, PBS, DMSNs, DSF@DMSNs, Zn-DMSNs and DSF@Zn-DMSNs dissolved in PBS (100 µL) at a DSF equivalent dose of 4.675 mg/kg were intratumorally injected into each mouse (n = 6) every 7 days. After injecting nanoparticles, body weight and tumor volume were measured every other day. After 14 days, these mice were sacrificed, and the tumor and major organs were dissected for weighing and imaging.

The tumors and organs were sectioned into slices for H&E, Ki67, and TUNEL staining. To determine the expression of LC3 and the intratumoral infiltration of functional CD4⁺ T cells and CD8⁺ T cells, tumor sections were stained by immunofluorescence (LC3, HMGB1, CRT, CD4⁺ and CD8⁺). This method was based on a previously reported method with some modifications [43]. To prove the immunomodulatory effects of DSF@Zn-DMSNs, the RNA of tumor tissues was extracted, and qPCR was performed to verify the relative expression of IFN γ , TNF α , and IL6.

4.20. *In vivo* antitumor therapy in a bilateral tumor model

A bilateral tumor model was established to verify the efficacy of DSF@Zn-DMSNs in activating the immune system. We injected 1×10^6 CT-26 cells during logarithmic phase into the left leg as the primary tumor and injected 5×10^5 CT-26 cells into the right leg as the distant tumor for each mouse after 5 days. We divided the 25 BALB/c mice into 5 groups: PBS, DMSNs, DSF@DMSNs, Zn-DMSNs and DSF@Zn-DMSNs (n = 5 in each group). We intratumorally injected assigned nanoparticles into every group at a DSF equivalent dose of 4.675 mg/kg on days 1 and 7 after planting the distant tumor. We measured the tumor volume and body weight every two days. On day 14, the mice were sacrificed, and the tumors were dissected, weighed and imaged.

4.21. *In vivo* DC maturation and T cell activation

The primary and distant tumors of the bilateral tumor model were prepared into a single-cell suspension by digestive juices containing 1 mg/mL collagenase and 150 U/mL Deoxyribonuclease I and filtered by a 70 µm filter net. Then, the single cells were collected for further staining by anti-CD45 Pacific blue, anti-CD11c PE, anti-CD80 FITC, anti-CD86 BV650, anti-CD3 FITC, anti-CD4 APC and anti-CD8 APC/Fire 750 before flow cytometry was carried out.

4.22. Statistical analysis

GraphPad Prism 8.0 software was used to draw graphs and perform statistical analysis. All data are presented as the mean \pm SD unless otherwise noted. Statistical analysis was performed with one-way ANOVA. When the *p* value < 0.05, the experimental results were statistically significant. All significant differences are represented by symbols. A *p* value < 0.05 was expressed as “*”. A *p* value < 0.01 was expressed as “**”. A *p* value < 0.001 was expressed as “***”. A *p* value < 0.0001 was expressed as “****”.

CRediT authorship contribution statement

Yang Yang: Writing – original draft, Conceptualization, Data curation, Formal analysis, Investigation, Methodology, Validation. **Yefei Zhu:** Writing – original draft, Data curation, Formal analysis, Investigation, Methodology, Validation. **Kairuo Wang:** Writing – original draft, Data curation, Investigation, Methodology, Validation. **Yunqiu Miao:** Formal analysis, Investigation, Thoughtful discussion. **Yuanyuan**

Zhang: Methodology. **Jie Gao:** Conceptualization, Supervision, Writing – review & editing. **Huanlong Qin:** Conceptualization, Supervision, Writing – review & editing, Funding acquisition. **Yang Zhang:** Conceptualization, Supervision, Writing – review & editing, Funding acquisition.

Declaration of competing interest

The authors declare that they have no competing interests.

All data needed to evaluate the conclusions in the paper are present in the paper and/or the Supplementary Materials. Additional data related to this paper may be requested from the authors.

Acknowledgements

We are grateful to Professor Jianlin Shi (Shanghai Institute of Ceramics, Chinese Academy of Sciences) for discussion and technical support. We gratefully thank Dr. Chen Qian for his indispensable contribution in the synthesis and property evaluation of nanoparticles and the polish of the manuscript. We also gratefully thank Mrs. Xinyue Wang for her indispensable contribution in the molecular biology experiments, pharmacodynamic, and immunological evaluation in animal experiments. This work was supported by the National Natural Science Foundation of China (Grant No. 81730102, 32271384), Shanghai Basic Research Program (Grant No. 20JC1411702), Shanghai Science and Technology Program (Grant No. 20ZR1456100).

Appendix A. Supplementary data

Supplementary data to this article can be found online at <https://doi.org/10.1016/j.bioactmat.2023.06.022>.

References

- J. Li, Y. Zhou, W. Zhao, J. Liu, R. Ullah, P. Fang, L. Fang, S. Xiao, Porcine reproductive and respiratory syndrome virus degrades DDX10 via SQSTM1/p62-dependent selective autophagy to antagonize its antiviral activity, *Autophagy* (2023) 1–18, <https://doi.org/10.1080/15548627.2023.2179844>.
- G. Chen, L.A. Emens, Chemoimmunotherapy: reengineering tumor immunity, *Cancer immunology, immunotherapy*, CII 62 (2013) 203–216, <https://doi.org/10.1007/s00262-012-1388-0>.
- L. Shefet-Carasso, I. Benhar, Antibody-targeted drugs and drug resistance—challenges and solutions, *Drug Resist. Updates : reviews and commentaries in antimicrobial and anticancer chemotherapy* 18 (2015) 36–46, <https://doi.org/10.1016/j.drug.2014.11.001>.
- Z. Yang, D. Gao, J. Zhao, G. Yang, M. Guo, Y. Wang, X. Ren, J.S. Kim, L. Jin, Z. Tian, X. Zhang, Thermal immuno-nanomedicine in cancer, *Nat. Rev. Clin. Oncol.* 20 (2023) 116–134, <https://doi.org/10.1038/s41571-022-00717-y>.
- L. Galluzzi, A. Buqué, O. Kepp, L. Zitvogel, G. Kroemer, Immunogenic cell death in cancer and infectious disease, *Nat. Rev. Immunol.* 17 (2017) 97–111, <https://doi.org/10.1038/nri.2016.107>.
- D.V. Krysko, A.D. Garg, A. Kaczmarek, O. Krysko, P. Agostinis, P. Vandenabeele, Immunogenic cell death and DAMPs in cancer therapy, *Nat. Rev. Cancer* 12 (2012) 860–875, <https://doi.org/10.1038/nrc3380>.
- R.H. Fang, A.V. Kroll, W. Gao, L. Zhang, Cell Membrane Coating Nanotechnology, *Adv. Mater. (Deerfield Beach, Fla.)* 30 (2018), e1706759, <https://doi.org/10.1002/adma.201706759>.
- A.K. Singh, J.P. McGuirk, CAR T cells: continuation in a revolution of immunotherapy, *The Lancet, Oncology* 21 (2020) e168–e178, [https://doi.org/10.1016/s1470-2045\(19\)30823-x](https://doi.org/10.1016/s1470-2045(19)30823-x).
- X. Wang, M. Li, K. Ren, C. Xia, J. Li, Q. Yu, Y. Qiu, Z. Lu, Y. Long, Z. Zhang, Q. He, On-demand autophagy cascade amplification nanoparticles precisely enhanced oxaliplatin-induced cancer immunotherapy, *Adv. Mater. (Deerfield Beach, Fla.)* 32 (2020), e2002160, <https://doi.org/10.1002/adma.202002160>.
- T. Jiang, X. Chen, X. Ren, J.M. Yang, Y. Cheng, Emerging role of autophagy in antitumor immunity: implications for the modulation of immunotherapy resistance, *Drug Resist. Updates : reviews and commentaries in antimicrobial and anticancer chemotherapy* 56 (2021), 100752, <https://doi.org/10.1016/j.drug.2021.100752>.
- R.K. Amaravadi, A.C. Kimmelman, J. Debnath, Targeting autophagy in cancer: recent advances and future directions, *Cancer Discov.* 9 (2019) 1167–1181, <https://doi.org/10.1158/2159-8290.Cd-19-0292>.
- B. Li, Z. Lei, B.D. Lichty, D. Li, G.M. Zhang, Z.H. Feng, Y. Wan, B. Huang, Autophagy facilitates major histocompatibility complex class I expression induced by IFN- γ in B16 melanoma cells, *Cancer immunology, immunotherapy*, CII 59 (2010) 313–321, <https://doi.org/10.1007/s00262-009-0752-1>.
- M. Zhou, Z. Wen, F. Cheng, J. Ma, W. Li, H. Ren, Y. Sheng, H. Dong, L. Lu, H.M. Hu, L.X. Wang, Tumor-released autophagosomes induce IL-10-producing B cells with suppressive activity on T lymphocytes via TLR2-MyD88-NF- κ B signal pathway, *Oncolimmunology* 5 (2016), e1180485, <https://doi.org/10.1080/2162402x.2016.1180485>.
- R. Gao, J. Ma, Z. Wen, P. Yang, J. Zhao, M. Xue, Y. Chen, M. Aldarouish, H.M. Hu, X.J. Zhu, N. Pan, L.X. Wang, Tumor cell-released autophagosomes (TRAP) enhance apoptosis and immunosuppressive functions of neutrophils, *Oncolimmunology* 7 (2018), e1438108, <https://doi.org/10.1080/2162402x.2018.1438108>.
- Z.F. Wen, H. Liu, R. Gao, M. Zhou, J. Ma, Y. Zhang, J. Zhao, Y. Chen, T. Zhang, F. Huang, N. Pan, J. Zhang, B.A. Fox, H.M. Hu, L.X. Wang, Tumor cell-released autophagosomes (TRAPs) promote immunosuppression through induction of M2-like macrophages with increased expression of PD-L1, *J. Immunol. Cancer* 6 (2018) 151, <https://doi.org/10.1186/s40425-018-0452-5>.
- M. Michaud, I. Martins, A.Q. Sukkurwala, S. Adjemian, Y. Ma, P. Pellegatti, S. Shen, O. Kepp, M. Scaozec, G. Mignot, S. Rello-Varona, M. Tailler, L. Menger, E. Vacchelli, L. Galluzzi, F. Ghiringhelli, F. di Virgilio, L. Zitvogel, G. Kroemer, Autophagy-dependent anticancer immune responses induced by chemotherapeutic agents in mice, *Science* 334 (2011) 1573–1577, <https://doi.org/10.1126/science.1208347>.
- F. Castoldi, E. Vacchelli, L. Zitvogel, M.C. Maiuri, F. Pietrocola, G. Kroemer, Systemic autophagy in the therapeutic response to anthracycline-based chemotherapy, *Oncolimmunology* 8 (2019), e1498285, <https://doi.org/10.1080/2162402x.2018.1498285>.
- D. Chen, Q.C. Cui, H. Yang, Q.P. Dou, Disulfiram, a clinically used anti-alcoholism drug and copper-binding agent, induces apoptotic cell death in breast cancer cultures and xenografts via inhibition of the proteasome activity, *Cancer Res.* 66 (2006) 10425–10433, <https://doi.org/10.1158/0008-5472.CAN-06-2126>.
- B. Cvek, V. Milacic, J. Taraba, Q.P. Dou, Ni(II), Cu(II), and Zn(II) diethyldithiocarbamate complexes show various activities against the proteasome in breast cancer cells, *J. Med. Chem.* 51 (2008) 6256–6258, <https://doi.org/10.1021/jm8007807>.
- X. Peng, Q. Pan, B. Zhang, S. Wan, S. Li, K. Luo, Y. Pu, B. He, Highly stable, coordinated polymeric nanoparticles loading copper(II) diethyldithiocarbamate for combinational chemo/chemodynamic therapy of cancer, *Biomacromolecules* 20 (2019) 2372–2383, <https://doi.org/10.1021/acs.biomac.9b00367>.
- W. Wu, L. Yu, Q. Jiang, M. Huo, H. Lin, L. Wang, Y. Chen, J. Shi, Enhanced tumor-specific disulfiram chemotherapy by *in situ* Cu(2+) chelation-initiated nontoxicity-to-toxicity transition, *J. Am. Chem. Soc.* 141 (2019) 11531–11539, <https://doi.org/10.1021/jacs.9b03503>.
- Z. Skrott, M. Mistrik, K.K. Andersen, S. Friis, D. Majera, J. Gursky, T. Ozdian, J. Bartkova, Z. Turi, P. Moudry, M. Kraus, M. Michalova, J. Vaclavkova, P. Dzubak, I. Vrobel, P. Pouckova, J. Sedlacek, A. Miklovicova, A. Kutt, J. Li, J. Mattova, C. Driessen, Q.P. Dou, J. Olsen, M. Hajdуч, B. Cvek, R.J. Deshaies, J. Bartek, Alcohol-abuse drug disulfiram targets cancer via p97 segregase adaptor NPL4, *Nature* 552 (2017) 194–199, <https://doi.org/10.1038/nature25016>.
- T. Sun, W. Yang, S.M. Toprani, W. Guo, L. He, A.B. DeLeo, S. Ferrone, G. Zhang, E. Wang, Z. Lin, P. Hu, X. Wang, Induction of immunogenic cell death in radiation-resistant breast cancer stem cells by repurposing anti-alcoholism drug disulfiram, *Cell communication and signaling, CCS* 18 (2020) 36, <https://doi.org/10.1186/s12964-019-0507-3>.
- X. Zhang, P. Hu, S.Y. Ding, T. Sun, L. Liu, S. Han, A.B. DeLeo, A. Sadagopan, W. Guo, X. Wang, Induction of autophagy-dependent apoptosis in cancer cells through activation of ER stress: an uncovered anticancer mechanism by anti-alcoholism drug disulfiram, *Am. J. Cancer Res.* 9 (2019) 1266–1281.
- Y. Hu, Y. Qian, J. Wei, T. Jin, X. Kong, H. Cao, K. Ding, The disulfiram/copper complex induces autophagic cell death in colorectal cancer by targeting ULK1, *Front. Pharmacol.* 12 (2021), 752825, <https://doi.org/10.3389/fphar.2021.752825>.
- C. Lv, W. Kang, S. Liu, P. Yang, Y. Nishina, S. Ge, A. Bianco, B. Ma, Growth of ZIF-8 nanoparticles *in situ* on graphene oxide nanosheets: a multifunctional nanoplatform for combined ion-interference and photothermal therapy, *ACS Nano* 16 (2022) 11428–11443, <https://doi.org/10.1021/acsnano.2c05532>.
- Y. Wei, N. Zhu, M. Lavoie, J. Wang, H. Qian, Z. Fu, Copper toxicity to *Phaeodactylum tricornutum*: a survey of the sensitivity of various toxicity endpoints at the physiological, biochemical, molecular and structural levels, *Biomaterials : an international journal on the role of metal ions in biology, biochemistry, and medicine* 27 (2014) 527–537, <https://doi.org/10.1007/s10534-014-9727-6>.
- J. Yue, Q. Mei, P. Wang, P. Miao, W.F. Dong, L. Li, Light-triggered multifunctional nanoplatform for efficient cancer photoimmunotherapy, *J. Nanobiotechnol.* 20 (2022) 181, <https://doi.org/10.1186/s12951-022-01388-8>.
- K.H. Müller, J. Kulkarni, M. Motskin, A. Goode, P. Winship, J.N. Skepper, M. P. Ryan, A.E. Porter, pH-dependent toxicity of high aspect ratio ZnO nanowires in macrophages due to intracellular dissolution, *ACS Nano* 4 (2010) 6767–6779, <https://doi.org/10.1021/nn101192z>.
- M. Huo, L. Wang, Y. Chen, J. Shi, Tumor-selective catalytic nanomedicine by nanocatalyst delivery, *Nat. Commun.* 8 (2017) 357, <https://doi.org/10.1038/s41467-017-00424-8>.
- S. Gao, H. Lin, H. Zhang, H. Yao, Y. Chen, J. Shi, Nanocatalytic tumor therapy by biomimetic dual inorganic nanzyme-catalyzed cascade reaction, *Adv. Sci.* 6 (2019), 1801733, <https://doi.org/10.1002/advs.201801733>.
- J. Liu, X. Zhao, W. Nie, Y. Yang, C. Wu, W. Liu, K. Zhang, Z. Zhang, J. Shi, Tumor cell-activated "Sustainable ROS Generator" with homogeneous intratumoral distribution property for improved antitumor therapy, *Theranostics* 11 (2021) 379–396, <https://doi.org/10.7150/thno.50028>.

- [33] K.L. Marie, A. Sassano, H.H. Yang, A.M. Michalowski, H.T. Michael, T. Guo, Y. C. Tsai, A.M. Weissman, M.P. Lee, L.M. Jenkins, M.R. Zaidi, E. Pérez-Guijarro, C. P. Day, K. Ylaya, S.M. Hewitt, N.L. Patel, H. Arnheiter, S. Davis, P.S. Meltzer, G. Merlino, P.J. Mishra, Melanoblast transcriptome analysis reveals pathways promoting melanoma metastasis, *Nat. Commun.* 11 (2020) 333, <https://doi.org/10.1038/s41467-019-14085-2>.
- [34] S. Wu, K. Zhang, Y. Liang, Y. Wei, J. An, Y. Wang, J. Yang, H. Zhang, Z. Zhang, J. Liu, J. Shi, Nanoenabled tumor systematic energy exhaustion via zinc (II) interference mediated glycolysis inhibition and specific GLUT1 depletion, *Adv. Sci.* 9 (2022), e2103534, <https://doi.org/10.1002/advs.202103534>.
- [35] R.F. Thorne, Y. Yang, M. Wu, S. Chen, TRIMming down autophagy in breast cancer, *Autophagy* 18 (2022) 2512–2513, <https://doi.org/10.1080/15548627.2022.2105557>.
- [36] M. Komatsu, Y. Ichimura, Physiological significance of selective degradation of p62 by autophagy, *FEBS Lett.* 584 (2010) 1374–1378, <https://doi.org/10.1016/j.febslet.2010.02.017>.
- [37] R. Vanzo, J. Bartkova, J.M. Merchut-Maya, A. Hall, J. Bouchal, L. Dyrskjøt, L. B. Frankel, V. Gorgoulis, A. Maya-Mendoza, M. Jäättelä, J. Bartek, Autophagy role (s) in response to oncogenes and DNA replication stress, *Cell Death Differ.* 27 (2020) 1134–1153, <https://doi.org/10.1038/s41418-019-0403-9>.
- [38] Y. Ma, L. Galluzzi, L. Zitvogel, G. Kroemer, Autophagy and cellular immune responses, *Immunity* 39 (2013) 211–227, <https://doi.org/10.1016/j.immuni.2013.07.017>.
- [39] S. Akira, S. Uematsu, O. Takeuchi, Pathogen recognition and innate immunity, *Cell* 124 (2006) 783–801, <https://doi.org/10.1016/j.cell.2006.02.015>.
- [40] C.A. Janeway Jr., K. Bottomly, Signals and signs for lymphocyte responses, *Cell* 76 (1994) 275–285, [https://doi.org/10.1016/0092-8674\(94\)90335-2](https://doi.org/10.1016/0092-8674(94)90335-2).
- [41] Q. Chen, T. Liu, S. Chen, Y. Luo, M. Ma, F. Xue, L. Zhang, W. Bao, H. Chen, Targeted therapeutic-immunomodulatory nanoplatform based on noncrystalline selenium, *ACS Appl. Mater. Interfaces* 11 (2019) 45404–45415, <https://doi.org/10.1021/acsami.9b15774>.
- [42] S. Zhang, F. Xie, K. Li, H. Zhang, Y. Yin, Y. Yu, G. Lu, S. Zhang, Y. Wei, K. Xu, Y. Wu, H. Jin, L. Xiao, L. Bao, C. Xu, Y. Li, Y. Lu, J. Gao, Gold nanoparticle-directed autophagy intervention for antitumor immunotherapy by inhibiting tumor-associated macrophage M2 polarization, *Acta Pharm. Sin. B* 12 (2022) 3124–3138, <https://doi.org/10.1016/j.apsb.2022.02.008>.
- [43] L. Pang, H. Jin, Z. Lu, F. Xie, H. Shen, X. Li, X. Zhang, X. Jiang, L. Wu, M. Zhang, T. Zhang, Y. Zhai, Y. Zhang, H. Guan, J. Su, M. Li, J. Gao, Treatment with mesenchymal stem cell-derived nanovesicle-containing gelatin methacryloyl hydrogels alleviates osteoarthritis by modulating chondrogenesis and macrophage polarization, *Adv. Healthc. Mater.* (2023), e2300315, <https://doi.org/10.1002/adhm.202300315>.